Articles in PresS. J Neurophysiol (April 19, 2017). doi:10.1152/jn.00826.2016

Cell-type specific changes in retinal ganglion cell function induced by rod death and cone reorganization in rats

Wan-Qing Yu[1], Norberto M. Grzywacz[1,2,3,4], Eun-Jin Lee[5]*+, Greg D. Field[6]*+

1. Neuroscience Graduate Program, University of Southern California, Los Angeles CA.

2. Department of Biomedical Engineering, University of Southern California, Los Angeles CA.

3. Department of Electrical Engineering, University of Southern California, Los Angeles CA.

4. Department of Neuroscience, Department of Physics, and Graduate School of Arts and Sciences, Georgetown University, Washington D.C.

5. Mary D. Allen Laboratory for Vision Research, USC Roski Eye Institute, Department of Ophthalmology, Keck School of Medicine University of Southern California, Los Angeles CA.

6. Department of Neurobiology, Duke University School of Medicine, Durham NC.

* These authors contributed equally.
+ To whom correspondence should be addressed.
eunjinl@usc.edu
field@neuro.duke.edu

Acknowledgements: We thank Jon Cafaro, Felice Dunn, Jeremy Kay, Nadav Ivzan, Arvind Iyer, Stephen Lisberger, Sneha Ravi, and Xiaoyang Yao for helpful discussions and comments on drafts. We thank Alexander Sher, Keith Mathieson, and Alan Litke for technical assistance. We thank the following funding sources: Whitehall Foundation (GDF), NIH-NEI R01-EY024567 (GDF), Karl Kirschgessner Foundation (GDF), VSoE Research Innovation Fund (EJL), and by National Science Foundation Grant 0310723 and NIH-NEI R01- EY016093 and EY11170 (NMG)

Abstract

We have determined the impact of rod death and cone reorganization on the spatiotemporal receptive fields (RFs) and spontaneous activity of distinct RGC types. We compared RGC function between healthy and retinitis pigmentosa (RP) model rats (S334ter-3) at a time when nearly all rods were lost, but cones remained. This allowed us to determine the impact of rod death on cone-mediated visual signaling -- a relevant time point because the diagnosis of RP frequently occurs when patients are night-blind, but daytime vision persists. Following rod death, functionally distinct RGC types persisted; this indicates that parallel processing of visual input remained largely intact. However, some properties of cone-mediated responses were altered ubiquitously across RGC types, such as prolonged temporal integration and reduced spatial RF area. Other properties changed in a cell-type specific manner such as temporal RF shape (dynamics), spontaneous activity, and direction selectivity. These observations identify the extent of functional remodeling in the retina following rod death, but prior to cone loss. They also indicate new potential challenges to restoring normal vision by replacing lost rod photoreceptors.

New and Noteworthy

This study provides novel and therapeutically relevant insights to retinal function following rod death, but prior to cone death. To determine changes in retinal output, we used a large-scale multi-electrode array to simultaneously record from hundreds of RGCs. These recordings of large-scale neural activity revealed that following the death of all rods, functionally distinct RGCs remain. However, the RF properties and spontaneous activity of these RGCs are altered in

a cell-type specific manner.

Introduction

Degeneration affects neural circuits throughout the brain. In some neurodegenerative diseases, dysfunction and death in a single cell type can cause a range of secondary effects across the circuit. For example, in retinitis pigmentosa (RP), the initial dysfunction and death of rod photoreceptors causes secondary structural changes in retinal circuits prior to the loss of all photoreceptors (*for review see* Krishnamoorthy et al. 2016; Puthussery and Taylor 2010). These changes include the retraction of bipolar cell dendrites, altered glutamate receptor expression, and cell migration (Dunn 2015; Gargini et al. 2007; Ji et al. 2012; Jones et al. 2016; Puthussery et al. 2009). To understand the functional consequences of these secondary changes, their impact on the signals sent from the retina needs to be determined. This will reveal the extent to which these changes in retinal circuitry induce subtle versus severe changes in retinal function; it will also likely guide the development of treatments for RP that restore vision more completely.

Retinal output, like that of many neural circuits, is carried by a diversity of cell types (Baden et al. 2016; Field and Chichilnisky 2007; Masland 2012; Sanes and Masland 2015). The mammalian retina consists of more than 20 (possibly ~40) types of retinal ganglion cells (RGCs). Each type has distinct receptive fields (RFs), light response properties, and spontaneous activity, which collectivity serve to signal distinct features of visual scenes to the brain. Rod loss may impact some RGC types more severely than others (Fransen et al. 2015; Margolis et al. 2008; Sekirnjak et al. 2011; Stasheff et al. 2011; Yee et al. 2014) and thus impair some aspects

of visual processing more than others. Thus, determining how rod death alters retinal function requires identifying and distinguishing changes in the RFs and other functional properties among different RGC types. This knowledge will provide clues to how rod death alters the function of different types of retinal interneurons (Euler and Schubert 2015; Toychiev et al. 2013; Trenholm et al. 2012; Trenholm and Awatramani 2015; Yee et al. 2012), and downstream visual areas (Chen et al. 2016; Dräger and Hubel 1978; Fransen et al. 2015)

A key time point to understand the impact of rod death on RGC function is prior to the loss of cones; many patients are diagnosed with RP when day-time vision persists, but they are nearly night-blind (Openshaw et al. 2008). Therefore, this is likely a time point near to which therapeutic interventions would begin. Knowing the extent to which rod death changes cone-mediated RGC light responses and RFs may lead to both earlier detection of RP and more effective therapies.

To determine changes in the function of distinct RGC types when rods have died, but cones remain, we used transgenic S334ter line 3 (S334ter-3) rats (Ji et al. 2012; Liu et al. 1999). This line exhibits relatively rapid rod death, but slow cone death (Ji et al. 2012; Ray et al. 2010). For example, at P60, the age animals were studied here, only 0.01% of rods remain, while there is no significant change in the number of cones (Ji et al. 2012; Mayhew and Astle 1997; Shin et al. 2016). Rod synaptic terminals have also likely degenerated because there is greatly reduced immunoreactivity for the presynaptic proteins synaptophysin and bassoon in the outer plexiform layer (Shin et al. 2015). Also, rod bipolar cells exhibit retracted dendrites, suggesting a loss of the glutamate release required to establish and maintain these synapses (Cao et al. 2015; Shin et

al. 2015). Therefore, S334ter-3 rats provide a temporal window in which the effects of rod death on cone-mediated RGC function can be determined. Furthermore, following rod death, cones in S334ter-3 rats reorganize their locations to form rings in the outer retina; cone cell bodies accumulate along the rings and avoid the ring centers (Ji et al. 2012; Yu et al. 2016; Zhu et al. 2013). The cones maintain at least some synaptic connections with second-order neurons (Shin et al. 2015). Thus, this animal model provides an opportunity to understand how rod death and concomitant changes in the outer retina impact cone-mediated vision.

We measured light responses and RFs from RGCs of S334ter-3 at P60 and compared them to age-matched wild-type (WT) animals. RGC light responses were measured by presenting several distinct visual stimuli while recording their spiking activity with a large-scale multielectrode array (MEA; Anishchenko et al. 2010; Field et al. 2010). This allowed recording from hundreds of RGCs simultaneously. These recordings facilitated a cell-type specific analysis of the impact of rod death across many RGC types. Some changes in RGC function were common across types; other changes were cell-type specific. This led to three primary conclusions. First, parallel processing in the retina remains largely intact after the death of rods and prior to the loss of cones. Second, the reorganization of cones disrupts the mosaic-like organization among the spatial RFs of each RGCs type. Third, rod loss does not only lead to a loss of rod-mediated signals among RGCs; it leads to altered temporal integration of cone-mediated responses, disruptions in the function of direction-selective RGCs, and differential changes in spontaneous spiking activity across RGC types. Collectively, these results point to several important changes in cone-mediated visual signaling that should be considered when testing strategies for rescuing vision in RP.

Materials and Methods

Animals. All procedures complied with and were prospectively approved by the Institutional Animal Care and Use Committee and the Department of Animal Resources at the University of Southern California or Duke University. Line 3 albino Sprague-Dawley rats homozygous for the truncated murine opsin gene (created a stop codon at Serine residue 334; S334ter-line-3) were obtained from Dr. Matthew LaVail (University of California, San Francisco, CA, USA). Homozygous S334ter-line3 female rats were crossed with Long Evans (Charles River, San Diego, CA, USA) male rats to produce heterozygous, pigmented offspring that were used as the model of RP in this study. S334ter-3 rats were sacrificed at post-natal (P) day 60 (8 rats from 4 litters). Age matched wild-type (WT) Long Evans rats were used as healthy control animals (7 rats from 3 litters). All rats were housed under 12-hour light/dark cycle with *ad lib.* access to food and water. Both sexes of control and S334ter-3 rats were used.

Immunohistochemistry. Retinas were obtained and processed as described previously (Ji et al. 2012; Lee et al. 2011). Eyes were enucleated from deeply anesthetized (Euthasol, 40 mg/kg, Fort Worth, TX, USA) dark-adapted rats prior to a second injection of Euthasol (40 mg/kg) to euthanize (overdose) the animal. The anterior segment and lens were removed and the eyecups were fixed in 4% paraformaldehyde in 0.1 M phosphate buffer (PB), pH 7.4, for 30 minutes to 1 hour at 4°C. Following fixation, the retinas were isolated from the eyecups and transferred to 30% sucrose in PB for 24 hours at 4°C. For fluorescence immunohistochemistry, 20 μm thick cryostat sections were incubated in 10% normal goat serum for 1 hour at room temperature. They were then incubated overnight with a rabbit polyclonal antibody directed against the mouse

middle-wavelength sensitive opsin (M-opsin, dilution 1:1000; kindly provided by Dr. Cheryl Craft, University of Southern California Roski Eye Institute) or a goat polyclonal antibody against short-wavelength sensitive opsin (S-opsin, dilution 1:1500, Santa Cruz Biotechnology, Santa Cruz, CA, # SC-14363). The antiserum was diluted in a phosphate buffered solution containing 0.5% Triton X-100 at 4°C. Retinas were washed in 0.01 M phosphate-buffered saline (PBS; pH = 7.4) for 45 minutes (3 x 15 minutes) and afterwards incubated for 2 hours at room temperature in carboxymethy-lindocyanine-3 (Cy3)-conjugated affinity-purified donkey anti-rabbit IgG (dilution 1:500, Jackson Immuno Labs, West Grove, PA, USA) or Alexa 488 anti-goat IgG (Molecular Probes, Eugene, OR; dilution 1:300). The sections were washed for 30 minutes with 0.1M PB and mounted on a glass slide with Vectashield mounting medium (Vector Labs, Burlingame, CA). For whole-mount immunohistochemical staining, the same procedure was used. The primary antibody incubation was for 2 days and the secondary antibody incubation was for 1 day.

Multielectrode array recordings. Rats were dark-adapted overnight. Eyes were enucleated from deeply anesthetized (ketamine - 100 mg/kg; KETASET, Fort Dodge, IA and xylazine - 20 mg/kg; X-Ject SA, Butler, Dublin, OH) dark-adapted rats following decapitation. The anterior portion of the eye, the lens, and the vitreous were removed in carbogen bubbled Ames medium (Sigma) at room temperature (22-24°C). During the dissection, retinal landmarks were used to track the orientation of retina (Wei et al. 2010). A dorsal piece of retina approximately centered along the vertical meridian was dissected and isolated from the pigment epithelium and sclera. This retinal location exhibits the highest level of M-opsin expression in cones (Ortín-Martínez et al. 2010). Only pieces that were well attached to the pigment epithelium after

removal of the vitreous were used. A piece of retina was placed RGC side down on a planar array of microelectrodes (Anishchenko et al. 2010; Field et al. 2010; Litke et al. 2004). The hexagonal array consisted of 519 electrodes with 30 μm spacing. Euthanasia, the retinal dissection, and mounting the retina on the MEA were all performed in a dark room with the aid of infrared converters and infrared illumination. Care was taken to eliminate any sources of visible light. During the recording, the retina was constantly perfused with Ames' solution (35°C) bubbled with 95% O_2 and 5% CO_2. Spikes recorded on the MEA were identified and sorted off-line using custom software as described previously (Field et al. 2007; Shlens et al. 2006). Automated spike sorting was first performed and then visually inspected on each electrode. When the user identified spike clusters that were missed by the automated procedure or single clusters that were fit with more than one Gaussian, the number of clusters was adjusted and the data were refit. Sorted (clustered) spikes were confirmed to arise from an individual neuron if they exhibited a temporal refractory period of 1.5 ms and an estimated contamination of <10% (Field et al. 2007).

Visual stimuli. Four visual stimuli were used in this study, checkerboard noise, drifting square-wave gratings, full-field light steps, and a spatially uniform and temporally static gray screen; parameters for each stimulus are detailed below. All visual stimuli were presented on an OLED display (Emagin, SVGA+ XL-OLED, Rev 3) controlled by custom software written in LISP, generously provided by Dr. E.J. Chichilnisky. The image of the display was focused on the photoreceptors through the mostly transparent MEA using an inverted microscope (Nikon, Ti-E, 4x objective). The mean intensity of all stimuli (static gray screen, white noise, drifting gratings and full-field light steps) was 7300 photoisomeriations per rod per second given the calibrated

power per unit area of the video display, the emission spectrum of the display, the spectral sensitivity of the rods, and a rod collecting area of 0.5 μm^2 (Baylor et al. 1984; Field and Rieke 2002, note: the effect of pigment self-screening was not included). The photoisomerization rate per cone was 6200 for M cones assuming a peak absorption at 510 nm and a collecting area of 0.37 μm^2. S opsin activation was negligible given the emission spectra of the video display. Binary checkerboard white noise stimuli that modulated the three primaries of the video display synchronously (each pixel was either "black" or "white" on any given frame) were used to estimate the spatiotemporal receptive fields of the recorded RGCs. Stimulus pixels (stixels) of the checkerboard were 20 x 20 μm or 60 x 60 μm along each edge and presented on a video display refreshing at 60.35 Hz. The smaller stixels were used to measure the spatial receptive field at high resolution. They were refreshed every 4 or 8 display frames (15.09 or 7.54 Hz). Larger stixels were used to estimate temporal RFs, and were refreshed every display frame (60.35 Hz). Square-wave gratings drifting in 8 directions with a spatial period of 512 μm and at temporal periods of 0.5 and 2 s were used to identify and classify DS ganglion cells (see below *Functional classification of RGCs*, Fig. 3A). Responses to these stimuli were also used to classify other retinal cell types based on their temporal modulation to the drifting grating (Fig. 3B). Full field light steps that cycled from white-to-gray-to-black-to-gray (3 s at each light level, 12 s per cycle) were presented to measure the polarity and kinetics of RGC responses to high-contrast light steps.

Receptive field measurements. The spatial and temporal receptive fields of RGCs were estimated by computing the spike-triggered average to a checkerboard noise stimulus (Chichilnisky 2001; Marmarelis and Naka 1972). The temporal RF was estimated by identifying stimulus pixels with

an intensity value that exceeded 4.5 robust standard deviations (SD) calculated over the intensity values of all stimulus pixels across all frames of the STA. The temporal evolution of these pixels was averaged to estimate the temporal RF. To estimate the spatial RF, the temporal RF was used as a template and the dot product between this template and each pixel of the STA across time was computed (Chichilnisky and Kalmar 2002; Field et al. 2010). This identified the spatial profile in the STA that evolved with the temporal receptive field. This procedure assumes the spatiotemporal RF is the product of independent spatial and temporal RFs (i.e. the RF is space-time separable). Singular value decomposition was also used to estimate (and separate) the rank-1 spatial and temporal RFs from the STA (Gauthier et al. 2009). Use of this alternative procedure did not change any conclusions in the paper. For a quantitative comparison, the time courses were fit with a difference of low-pass filters and three features were extracted from these fits: time-to-peak, time-to-zero crossing, and degree of transience (DoT; Fig. 8A, top-right panel)(Chichilnisky and Kalmar 2002; Field et al. 2007).

Binary response map. A binary response map was generated across RGC receptive fields to analyze the uniformity of visual sensitivity across space (Fig. 2). This map was calculated by overlaying individual binarized STAs. STAs were binarized by a threshold set to 4.5 SDs of the distribution of STA intensity values. For pixel values larger than 4.5 SD from the mean, the pixel location was labeled 1, otherwise 0.

Analyzing spatial RF shapes and sizes. RF shapes were analyzed by calculating a convexity index (Fig. 7B). This index was the ratio of the spatial RF area to the area of the convex hull of the spatial RF. For a perfectly Gaussian RF, this index will be approximately equal to one, but

substantially smaller than one for an RF that is has a ring-like or arc-like shape. The spatial RF was estimated from the spatial component of the STA as described above. A region of interest (ROI) was defined around the spatial RF to exclude noisy stimulus pixels that could cross threshold far from the RF. This ROI was generated by downsampling the original high-resolution (20x20 μm) STA by 4-fold (every four stixels in the STA were averaged to form one stixel) and blurred with a 2-D Gaussian function (SD = 8 stixels). Once the ROI was selected, significant stixels were extracted from the down sampled (but not blurred) STA by a threshold set to 4.5 SD above or below the mean stixel intensity. A convex hull was then generated from these significant stixels. RF sizes (Fig. 7E & F) were also calculated from the down-sampled STA (without blurring) as the total area of all stixels that exceeded 4.5 SD above or below the mean. Note, DS-RGCs and ON Brisk Sustained RGCs were excluded from this analysis because the spatial RFs did not consistently exhibit a signal-to-noise ratio sufficient to reliably estimate the shape.

Functional classification of RGCs. RGCs were classified based on their light responses and intrinsic spiking dynamics. The classification was serial; in each parameter space, one type of RGC was identified, these cells were then removed from the data, and another type was identified among the remaining RGCs in a new parameter space (Fig. 3). RGCs of a given type were first selected "by hand" by drawing a boundary in a 2- or 3-dimensional parameter space. To objectively define the boundary separating an RGC type from all other cells, a two-Gaussian mixture model (in two or three dimensions) was fit to capture the distribution of points in the parameter space (Fig. 3). The initial conditions of this fit were provided by the by-hand classification.

The same parameter spaces were used at each step in the classification procedure for both WT and S334ter-3 retinas. The first step isolated DS-RGCs from all other recorded cells (Fig. 3A & E). DS-RGCs were distinguished based on the strength of their direction selective index (DSI) computed from rapidly and slowly drifting square-wave gratings (temporal periods = 0.5 s and 2 s, respectively). The next step separated ON from OFF RGCs by the sign of largest magnitude peak in their temporal RFs, estimated from checkerboard noise (not shown). Among ON RGCs, ON brisk sustained RGCs were isolated first by comparing their responses to rapidly and slowly drifting gratings and to the DoT of their temporal RF (Fig. 3B & F). ON brisk sustained RGCs formed a clear cluster in this parameter space in S334ter-3 and WT retinas (Fig 3B & F, red circles). Subsequently, ON brisk transient (Fig 3C & G) and ON small transient (Fig 3D & H) were identified using the parameter spaces shown in Figure 3. After classifying these ON RGC types, OFF RGCs were classified. The order and parameter spaces are illustrated in Figure 3, with OFF brisk sustained (Fig 3I & M), OFF brisk transient (Fig 3J & N), OFF small transient (Fig 3K and O), and OFF sluggish cells (Fig 3L & P) classified in that order. This naming convention for functionally distinct RGC types is largely taken from previous work in the rabbit and cat retinas (Amthor et al. 1989a, b; Caldwell and Daw 1978; Cleland et al. 1973; Cleland and Levick 1974). Different naming conventions have been used previously in the rat (Heine and Passaglia 2011), but we viewed the convention used in the rabbit as better describing the functional distinctions between RGC types measured in this study.

This classification order was used because it provided a large separation between clusters defining each cell type at each classification step. Because we did not exhaustively search all

possible parameter spaces and classification orders, we cannot claim the parameter spaces or classification order used are optimal. However, this classification procedure did yield robust results across experiments in both WT and S334ter-3 retinas (Fig. 3). Changing the classification order or using alternative parameter spaces revealed the same basic RGC types but with a higher miss-classification rate as judged by RGCs with clearly distinct response properties and irregular cell spacing or mosaic violations among the spatial RFs. Using these alternative classifications did not qualitatively change any of the results reported here.

Matching RGC types between WT and S334ter-3 retinas. A minimal mapping algorithm (Ullman, 1979) was used to match RGC types one-to-one between WT and S334ter-3 retinas (Fig. 5). The most plausible matching was determined by minimizing the sum of the distances between selected properties of matched pairs. Two functional properties of RGCs were analyzed: temporal RFs and responses to full-field light steps. To match temporal RFs (Fig 5A-D), they were first normalized to unit magnitude and then averaged across all RGCs of a type. The sum of dot products was calculated for each possible pairing of mean temporal RFs from WT and S334ter-3 RGC types. With seven RGC types to pair (DS-RGCs were excluded from this analysis) there were 5040 summed dot products calculated. The maximum of these summed dot products was chosen as the best match. This corresponds to minimizing the angular distances between pairs. The z-score for this match was 3.02, relative to the distribution of all 5040 summed dot products.

Responses to full-field light steps were analyzed similarly to the temporal RFs (Fig. 5E). The peri-stimulus time histogram (PSTH) for each RGC in response to this stimulus was normalized

307 to unit magnitude and then averaged over RGCs of a type separately for WT and S334ter-3
308 retinas. The sum of dot products between mean PSTHs for all possible pairings was calculated
309 and the maximum was selected as the best match. The largest sum of these dot products had a z-
310 score of 3.23 relative to the distribution of 5040 summed dot products.
311
312 *Analysis of spike shapes.* One line of evidence that RGC types were reliably matched between
313 S334ter-3 and WT retinas was based on spike shape (Fig. 6). In particular, RGC types with
314 similar light response properties between WT and S334ter-3 retinas also exhibited the greatest
315 similarities in the shape of their average spike waveform. To estimate the spike waveform shape
316 of each individual RGC, spikes detected on the MEA were sampled at 20 kHz. For a given
317 RGC, spike waveforms were averaged across the two electrodes with the highest spike amplitude
318 for that cell. Cells with their largest amplitude spike waveforms recorded on electrodes at the
319 edge of the MEA were excluded from the analysis. These cells frequently had small signals on
320 those electrodes, presumably because the cell body was some distance from the MEA edge. For
321 RGCs of a given type, the spike waveforms were averaged across cells to generate the average
322 spike waveform for that type. These waveforms were accumulated over each RGC type in seven
323 WT and five S334ter-3 retinas. Three WT retinas were used in this analysis that were not used
324 elsewhere in the manuscript because they were recorded at ages other than P60; their RGCs were
325 classified as described above. The average spike spaces for each RGC type were then compared
326 using principal components analysis (PCA); average spike waveforms were analyzed separately
327 for ON and OFF RGCs (Fig. 6). Specifically, PCA provided a low-dimensional space in which to
328 represent the average spike waveforms for each RGC type from each recording (Figs. 6C & F),
329 which facilitated comparing their shapes. Spike waveforms that were similar in shape clustered

together in the low-dimensional space identified by PCA, indicating spike waveforms across recordings were similar within an RGC type (for both WT and S334ter-3 animals) and distinct across RGC types.

RGC locations from electrophysiological images. The electrophysiological image (EI) is the average electrical activity of a neuron produced across the electrode array (Field et al. 2009; Litke et al. 2004; Petrusca et al. 2007). After the spikes from a given neuron were isolated on a source electrode, the electrical activity in a time window 0.5 ms before to 3 ms after the spike was averaged over all spikes. Because the spiking activity of any given cell is largely independent from all other cells, the average electrical activity across the array reveals a unique spatiotemporal electrical "footprint" for every cell, reflecting its position, width of dendritic arbor, and axon trajectory registered to the electrode array. The EI, excluding the axon, was used to estimate the soma location of RGCs over the array by fitting a two-dimensional Gaussian. Electrodes dominated by axonal signals were excluded by identifying manually those electrodes with triphasic voltage waveforms in the EI (Litke et al. 2004). The center of the Gaussian was taken as a representation of RGC position (Li et al. 2015). Note this position need not be registered with an electrode, so the regular spacing between electrodes does not enforce regularity upon the estimated RGC locations.

Quantifying the Tuning of DS-RGCs. To quantify the directional tuning of DS-RGCs (Fig. 9), the average firing rates for gratings drifting in 8 directions (temporal period = 0.5 s, spatial period = 512 μm) were fitted with von-Mises function (Eq. 1; (Oesch et al. 2005)), the parameters of the function were estimated using maximum likelihood methods (Berens 2009) and the peak and full

width at half height were computed (Eq. 2; Elstrott et al. 2008). Direction tuning curve shape was insensitive to increasing the temporal period of the drifting gratings to 2 s. Circular statistics were used to calculate the circular skewness of individual DS tuning curves and Rao's spacing test for the nonuniformity of preferred tuning distribution (Berens 2009).

$$response = \frac{Aexp(\kappa cos((x-u)\pi/180))}{exp(\kappa)} \quad (1)$$

$$fwhh = 2acos(\frac{1}{\kappa}log(\frac{exp(\kappa)+exp(-\kappa)}{2})) \quad (2)$$

A is the maximum response, *u* is the preferred direction in radians and was determined by the vector sum of the normalized responses across the 8 presented grating directions, and *k* is the concentration parameter accounting for tuning width.

Statistical analysis. Unless noted otherwise, the two-tailed Mann-Whitney test was used to compare WT and RP datasets, and significance was determined at $p < 0.05$; data are presented as means ± SD. In Figure 7C, D and F, linear regression was used to fit the data. All statistics were performed using R 3.2.4 (R Foundation for Statistical Computing; https://www.R-project.org).

Results

The primary goal of this study was to determine the impact of rod photoreceptor death on cone-mediated signaling among RGCs. First, we show RGC spatial RFs are irregular due to the

reorganization of cones in this animal model of RP. Second, despite the nearly complete loss of rods, RGC types persist and can be matched to cell types in WT retinas. These RGC types exhibit a mosaic organization, indicating they correspond to morphologically distinct types. Third, we show both common and cell-type specific changes in the spatiotemporal RF structure, direction selectivity, and spontaneous activity caused by the loss of rods and reorganization of cones.

Photoreceptor remodeling leads to distorted RGC receptive fields

S334ter-3 rats exhibit progressive photoreceptor degeneration that begins with rods and eventually leads to cone death (Ji et al. 2012; Liu et al. 1999). Most rods die by P30, while cone loss is minimal prior to P180 (Ji et al. 2012). Between rod and cone death, cones reorganize to form rings in the outer retina (Ji et al. 2012). To determine the extent of this reorganization at P60, the age at which RGCs were recorded in this study, WT and S334ter-3 retinas were immunolabeled for opsins. M-opsin immunoreactivity in WT animals revealed cones that were vertically aligned and homogeneously organized with uniform spacing across the retina, consistent with previous studies (Figs. 1A & C; Garcia-Ayuso et al. 2013; Ji et al. 2012). In contrast, M-opsin immunoreactivity in S334ter-3 retinas revealed that cones lost their vertical orientation, lying flat against the outer retina with shorter and distorted outer segments (Fig. 1B). Consistent with previous observations at P90 (Ji et al. 2012), the cones also exhibited a ring-like spatial organization, leaving large holes with few or no cones (Fig. 1D). A similar pattern was observed with S-opsin immunoreactivity (data not shown; Ji et al. 2012).

To determine the consequences of these structural changes on the spatial RFs of RGCs, WT and S334ter-3 rat retinas were recorded on a large-scale MEA while presenting visual stimuli

(Anishchenko et al. 2010; Litke et al. 2004). Checkerboard noise stimuli were presented to estimate the spatiotemporal RFs of RGCs by computing the spike-triggered average (STA) stimulus (Chichilnisky 2001). In WT retinas, the RFs of ON and OFF RGCs exhibited a Gaussian-like shape (Fig. 2A). In contrast, RFs from S334ter-3 retinas exhibited anomalous spatial structures; they tended to form arcs, partial rings, and sometimes complete rings (Fig. 2B). This structure was reminiscent of that observed in the cone mosaic (Fig. 1D). Indeed, when RFs of individual RGCs were summed together to generate a binary map of spatial sensitivity across the retina, the map revealed ring-like regions that were responsive to light that encircled large regions that were insensitive to light (Fig 2D; *see Materials and Methods*). This functional map of light sensitivity reproduced the pattern exhibited by the cone outer segments in S334ter-3 retinas (Fig. 2D, inset). In comparison, the maps of spatial sensitivity did not exhibit ring-like patterns in WT retinas (Fig. 2C).

To determine whether anatomical holes in the cone mosaic and functional holes in RGC light sensitivity matched in size, the diameters of rings observed anatomically and functionally were compared by fitting each ring with an ellipse. The mean diameter of these ellipses (geometric mean of the major and minor axes) was not significantly different between anatomical and functional rings (anatomical rings: 274 ± 66 μm; physiological rings: 243 ± 72 μm; $p = 0.3204$).

The regions in S334ter-3 retinas with little to no light sensitivity were not caused by a failure to record from RGCs in those regions. The total number of recorded RGCs (classified and unclassified) in each WT and S334ter-3 experiment was not significantly different (WT: 291 ± 28, $n = 4$, RP: 350 ± 18, $n = 5$; $p = 0.1905$), indicating that the efficiency of recording from

RGCs was similar in S334ter-3 and WT retinas. In addition, estimates of RGC soma locations from the electrical images of recorded RGCs (*see Materials and Methods*) indicated that total RGC density was unchanged in areas with low visual sensitivity in S334ter-3 retinas (low sensitivity: 551 ± 51 cells/mm^2, whole area: 556 ± 47 cells/mm^2, n = 5, p = 0.8413; Chan et al. 2011). Therefore, the gaps in light sensitivity in the recorded retinas were caused by the reorganization of cones into rings.

Functionally distinct RGC types remain after rod death

The results of Figure 1 & 2 demonstrate a structural and functional reorganization in the outer retina, caused by rod death and cone reorganization. To determine the consequences of these changes on the many functionally diverse RGC types in the mammalian retina necessitates a cell-type specific analysis (Della Santina et al. 2013; Ou et al. 2015; Sanes and Masland 2015; Yee et al. 2014). Therefore, we first establish a method for functionally classifying RGCs from these MEA recordings and show that functionally distinct RGC types persist after the loss of nearly all rods.

A semi-supervised classification of RGCs based on their light responses was applied to WT retinas (Fig. 3A-D & I-L, *see Materials and Methods*). RGCs were classified in a serial manner, in which a distinct type was isolated from all other RGCs at each step in the classification. This approach allowed ~40% of RGCs in WT retinas to be classified into distinct types (Fig. 3A-D, I-L, WT: 42.2 ± 1.4%, RP: 42.4 ± 1.4%). Specifically, we identified ON-OFF direction selective RGCs, functionally symmetric pairs of ON and OFF brisk sustained (BS) cells, ON and OFF brisk transient (BT) cells, ON and OFF small transient (ST) cells, and finally OFF sluggish RGCs. To validate the output of this classification, each identified type exhibited an

443 approximate tiling of RFs over space and regular spacing of RGC locations (Fig. 4A, C, E & G).
444 These features indicate that each functionally defined type corresponds to a morphologically
445 distinct RGC type because they also exhibit regularly spaced cell bodies and approximate tiling
446 between neighboring dendritic fields (Dacey 1993; Vaney 1994; Wassle et al. 1981).
447 Additionally, this tiling arrangement of RFs indicates that each RGC type could not be further
448 subclassified (Devries and Baylor 1997; Field et al. 2007).
449
450 We used the identical classification approach to reveal functionally distinct RGC types in
451 S334ter-3 retinas (Fig. 3E-H, M-P). Specifically, each classification space that identified an RGC
452 type in WT retinas, also identified an RGC type in S334ter-3 retinas. To check that RGC types
453 identified in S334ter-3 retinas corresponded to morphologically distinct RGC types, their spacing
454 was analyzed (Fig. 4B, D, F & H; Dacey 1993; Vaney 1994; Wassle and Riemann 1978). RGC
455 locations were estimated by the location of their electrical signals on the MEA. Note that these
456 locations were not fixed to the grid of electrodes, thus regular electrode spacing did not enforce
457 regular RGC spacing (*see Materials and Methods*). The distribution of nearest-neighbor
458 distances (NNDs) for RGC locations indicated that they were not consistent with a random
459 distribution (Fig. 4B, D, F & H, histograms). Specifically, the dearth of short distances supported
460 the existence of an exclusion zone around each RGC within a type, but not across types (Fig. 4,
461 magenta curves). In addition, the clear peaks in each NND distribution indicates a tendency
462 toward regular spacing. This suggests these functionally defined RGC types corresponded to
463 morphologically distinct types. Note, the cone reorganization disrupted the spatial structure of
464 individual RFs and thus also disturbed the tiling of neighboring RFs in S334ter-3 retinas (Fig 4).
465

While the total number of cells in each type varied across preparations, the functional classification of RGCs in WT and S334ter-3 retinas was consistent (Table 1). Seven types of RGCs emerged in WT and S334ter-3 retinas in addition to four types of ON-OFF direction selective RGCs (one type for each cardinal direction, data not shown).

Matching RGC types between WT and S334ter-3 retinas

To determine how rod death and the reorganization of cones impacts different RGC types, they must be matched between WT and S334ter-3 retinas. We matched RGC types based on their classification order. The validity of this matching is supported by four lines of evidence. The first line of evidence is the parameter spaces used to identify each RGC type in WT and S334ter-3 retinas were identical (Fig 3). Furthermore, the distributions of RGCs in these parameter spaces were similar between WT and S334ter-3 animals (e.g., compare Fig 3A with 3E, 3B with 3F, etc). This suggests that while rod death perturbed RGC function, these perturbations were relatively small compared to the functional distinctions between RGC types.

The second line of evidence is based on matching cell types by the dynamics of their temporal RFs (Fig 5A-D). RGC temporal RFs indicate how visual input is integrated in time; they were estimated from the STAs (*see Materials and Methods*). To choose the best matching between RGC types in WT and S334ter-3 retinas, a minimal mapping algorithm was applied to the average temporal RF of each RGC type; DS-RGCs were not included in this analysis. This algorithm finds the set of matches between elements from two conditions that are most similar (*see Materials and Methods*; Grzywacz and Yuille 1988; Ullman 1979). The minimal mapping algorithm indicated that the best matching was the same as that indicated by the classification

order. This result supports the conclusion that RGC types were correctly matched between WT and S334ter-3 retinas.

The third line of evidence is based on matching RGC types by their responses to full-field light steps (Fig. 5E). This response feature provided a more independent matching than the previous two lines of evidence because full-field light steps were (1) not used in the classification and (2) the responses to this stimulus were not well predicted by temporal RF dynamics; full-field light steps stimulate center and surround simultaneously, engaging RF nonlinearities (Sagdullaev and McCall 2005). The responses to full-field light steps were summarized by generating a peri-stimulus time histogram (PSTH). These histograms were averaged across cells of a type. The best matching was identified by the minimum mapping algorithm applied to these histograms (Fig 5E; *see Materials and Methods*). The matching of cell types by this method was identical to the two previous methods.

The three previous lines of evidence were all based on responses to visual stimuli. However, rod death and the reorganization of cones may cause the response properties of one RGC type to mimic those of another. Thus, the fourth line of evidence is based on spike shape, an intrinsic neuronal property. If photoreceptor degeneration minimally perturbs ion channel expression patterns among RGCs, then the spike shapes of each RGC type should be similar within types and different across types for WT and S334ter-3 retinas. To test this, the spike shape for each RGC type was estimated by averaging the extracellularly recorded spike waveforms across all cells of a type in each recording (*see Materials and Methods*). This analysis was limited to non-

511 DS-RGCs. The mean spike shapes revealed subtly different dynamics across cell types and in
512 S334ter-3 retinas (Fig. 6A, B, D & E).
513
514 To determine whether these differences were systematically preserved across healthy and
515 S334ter-3 retinas, PCA was used to identify a subspace for viewing the spread in spike shapes
516 across recordings (Fig 6C & F). For the three ON cell types, spike waveforms clustered by type
517 in a subspace defined by the first two principal components (Fig 6C, note: filled symbols are RP
518 recordings). The first principal component separated ON brisk sustained cells, while the second
519 component separated brisk transient from small transient cells. For the four OFF RGC types,
520 spike waveforms clustered by types in a subspace defined by the first three principal components
521 (Fig 6F). When omitting the OFF sluggish cells from the classification, PCA yielded a similar
522 clustering of the OFF brisk sustained, brisk transient and small transient cells as that produced by
523 the corresponding ON RGC types (Fig 6F, inset). Therefore, spike shapes were consistent
524 between WT and S334ter-3 retinas within RGC types and systematically different across types.
525 This further supports the conclusion that RGC types were correctly matched between WT and
526 S334ter-3 retinas.
527
528 To summarize, the classification parameter spaces, the temporal RFs, responses to full-field light
529 steps, and spike shapes all indicated the same matching of RGC types between WT and S334ter-
530 3 retinas. This indicates that RGC types persisted and could be analyzed independently after rod
531 death and the reorganization of cones.
532
533 **Rod death and cone reorganization alters RF size and shape**

534 The distributions of spatial RF sizes and shapes summarize the resolution and regularity with
535 which visual scenes are sampled by RGCs. Changes in the size or shape of spatial RFs indicates
536 altered visual signaling. We therefore determined how the size and shape of cone-mediated
537 spatial RFs were altered by rod death in specific RGC types. This analysis led to three
538 conclusions: (1) the distribution of RF shapes changed uniformly across all examined RGC
539 types; (2) the larger variation in RF shape among RGCs from S334ter-3 animals was consistent
540 with the reorganization of cones; (3) RGC types with larger spatial RFs exhibited larger changes
541 in RF size than those with smaller spatial RFs.
542
543 To analyze changes in RF shape, a convexity index (CI) was computed for the spatial RFs of
544 each RGC (Fig 7A & B). High indices correspond to approximately Gaussian-shaped RFs while
545 arc-like RFs will have low indices. In WT retinas, convexity indices were close to one on
546 average and the distributions of convexity indices were similar for all types examined (Fig. 7B,
547 black distributions). In contrast, S334ter-3 retinas exhibited distributions of convexity indices,
548 with lower mean values (Fig. 7B, green distributions). The distributions were similar across RGC
549 types in S334ter-3 retinas, indicating that rod death had a similar impact on RF shape across cell
550 types.
551
552 The distribution of convexity indices in S334ter-3 also exhibited higher variance than in WT
553 (Fig. 7B), indicating that some individual RGCs were impacted by rod death and the
554 reorganization of cones more than others. A possible explanation is that RGCs located near the
555 center of a hole in the cone mosaic receive input from many cones that moved to the rim of a
556 ring. These RGCs would exhibit non-convex RF shapes such as arcs. In contrast, RGCs located

557 near the rim of a ring may receive input from cones that migrate less far and the RFs of these
558 RGCs will remain more Gaussian. To test this possibility, the relationship between RF shape
559 and RF displacement was compared for each RGC (Fig. 7C &D). RF displacement was
560 estimated as the median distance from the RF center of mass to the RGC location (as estimated
561 from the electrical image of the RGC, *see Materials and Methods*). Convexity indices and RF
562 displacements were negatively correlated in S334ter-3 retinas (Fig. 4D, $r^2 = 0.23$, $\beta = -141.4$, $p <$
563 0.00001), but not in WT retinas (Fig. 4C, $r^2 = 0.002$, $\beta = -33.6$, $p = 0.4947$). This analysis
564 indicates that changes in cone-mediated RF shape are largely due to the reorganization of cones.
565
566 Finally, we found that RGCs with larger RFs exhibited greater changes in size compared to those
567 with smaller RFs. Spatial RF sizes were computed for each RGC type in WT and S334ter-3
568 retinas (*see Materials and Methods*). Consistent with previous studies (Hammond 1974; Heine
569 and Passaglia 2011; Petrusca et al. 2007), RF size depended strongly on RGC type (Fig. 7E).
570 OFF brisk transient RGCs had the largest RFs, while OFF sluggish RGCs had the smallest (Fig.
571 7B). In S334ter-3 retinas, RF sizes decreased significantly in all types relative to WT ($p <$
572 0.00001 for all the types). However, their relative order (largest to smallest) was maintained (Fig.
573 7E). Moreover, the shrinkage of the mean RF was proportional to its size (Fig. 7F, $r^2 = 0.91$, $p =$
574 0.002). Therefore, while changes in spatial RF shape were largely independent of cell types,
575 changes in RF size were cell-type dependent.
576

577 ## Rod death prolongs temporal integration of RGCs

578 Just as each RGC type has a distinct spatial RF, each type integrates visual signals with distinct
579 temporal dynamics. These dynamics determine the range of temporal frequencies that readily

drive responses in RGCs. Human patients with RP exhibit diminished temporal vision becoming less sensitive to high temporal frequencies (Dagnelie and Massof 1993), which may be explained by changes in RGC temporal RFs. Therefore, we determined how temporal RF dynamics were affected by rod death (Fig. 8).

For all non DS-RGC types, the dynamics of the temporal RF was slower (exhibited prolonged temporal integration) in S334ter-3 than in WT retinas (Fig. 8A, $p < 0.0001$ for all the types). For a quantitative comparison, the temporal RFs were fit with a difference of low-pass filters and three features were extracted from these fits: time-to-peak, time-to-zero-crossing, and degree of transience (DoT) (Fig. 8A, top-right panel).

The time-to-peak of the temporal RF corresponds to response latency (Chichilnisky and Kalmar 2002; Field et al. 2007). Analysis of the time-to-peak indicated that rod death leads to increased response latencies among all RGCs, but the magnitude of the change depends on RGC type (Fig. 8B, $p < 0.0001$ for all the types). Specifically, in S334ter-3 retinas, the mean time-to-peak was delayed 36 ms compared to WT. OFF sluggish RGCs exhibited the largest change (42 ms, 29.3%) while OFF small transient RGCs exhibited the smallest change (25 ms, 25.2%).

Time-to-zero crossing of the temporal RF is related to the time of maximum firing rate in response to a step in light intensity (Field et al. 2007). Similar to the time-to-peak, all RGC types in S334ter-3 retinas had longer time-to-zero-crossings than in WT (Fig. 8C, $p < 0.0001$ for all the types). The mean time-to-zero crossing was delayed 67 ms compared to WT. However, the magnitude of the delay depended on RGC type, with the OFF brisk sustained RGCs being

603 affected the most (95 ms, 75.8%) and OFF brisk transient RGCs the least (32 ms, 21.0%, Fig.
604 8C).
605
606 DoT quantifies the biphasic nature of the temporal RF and indicates whether the temporal
607 filtering of visual input is lowpass or bandpass (e.g., a high biphasic index indicates strongly
608 bandpass temporal integration). The impact of S334ter-3 on DoT depended on RGC type (Fig.
609 8D, $p = 0.6743$ for OFF sluggish, $p = 0.4402$ for OFF brisk transient, and $p < 0.0001$ for all other
610 types). In particular, OFF small transient RGCs became less biphasic while ON small transient,
611 OFF brisk sustained, and ON brisk sustained cells became more biphasic; the DoT of OFF
612 sluggish and OFF brisk transient cells did not change significantly.
613
614 These results indicate that rod degeneration generally prolonged the temporal integration of
615 RGCs. However, the magnitude of prolongation and changes in the dynamics of temporal
616 integration depended on RGC type.
617
618 **Impact of rod death on DS-RGCs**
619 DS-RGCs signal visual motion to the brain (Barlow and Hill 1963; Grzywacz and Amthor 1993;
620 Oyster and Barlow 1967; Vaney et al. 2012). They are likely important for the optokinetic reflex
621 and may play a role in shaping cortical motion processing (Cruz-Martín et al. 2014; Yoshida et
622 al. 2001). Furthermore, direction selectivity is the result of a precisely wired circuit within the
623 retina (Briggman et al. 2011; Demb 2007; Ding et al. 2016; Hoggarth et al. 2015). Therefore,
624 changes in DS-RGC function induced by rod death may provide a “canary in the coal mine” for

observing perturbations to retinal circuits and may be predictive of behavioral deficits related to motion processing.

We first tested whether DS-RGCs persisted after the death of rods and reorganization of cones. The reorganization of the outer retina did not significantly decrease the proportion of RGCs identified as direction selective in S334ter-3 retinas compared to WT (WT: 17.4 ± 0.5%, RP: 15 ± 1.0%, Pearson's Chi-square test, χ^2= 2.5698, df = 1, p = 0.1089). This indicates that rod death and cone reorganization do not cause a rewiring in the inner retina that eliminates direction selectivity.

To test for more subtle changes in DS-RGC function, the shape of their direction tuning functions were compared between S334ter-3 and WT retinas (Fig 9A-C). DS-RGC tuning curves were measured using square-wave gratings that were drifted in eight directions (*see Materials and Methods*). Tuning curves were broader in S334ter-3 retinas, indicating that individual cells were less precisely direction tuned (Fig. 9B, one-tailed Mann-Whitney test, p = 0.0013). To test for changes in tuning curve symmetry, the circular skewness of the tuning curve was calculated for each DS-RGC (*see Materials and Methods*). The distribution of these skewness values was broader in S334ter-3, indicating more DS-RGCs with asymmetric tuning curves (Fig. 9C, WT: -0.005+0.05, RP: 0.001+0.09 (means ± SD), one-tailed F-test, p < 0.0001). These analyses suggest that cone reorganization may disrupt the precision and regularity of DS-RGC tuning. A change in in the temporal integration of DS-RGCs, like that observed for non DS-RGCs (Fig. 8), may also contribute to changes in direction tuning width. However, this is unlikely to fully explain these observations because the expected change in

temporal integration (~50%, as estimated from non DS-RGCs in Fig. 8) is much less than the increase in the temporal period of drifting gratings (~400%) required to match the increase in tuning width observed in DS-RGCs (data not shown).

If the tuning of individual DS-RGCs is perturbed by the reorganization of cones, this suggests that the direction preferences among populations of DS-RGCs may no longer lie along four cardinal directions (Elstrott et al. 2008; Oyster and Barlow 1967). We measured the direction tuning across populations of simultaneously recorded DS-RGCs in WT and S334ter-3 retinas. In WT retinas, population tuning preferred four cardinal directions (Fig. 9D). In S334ter-3 retinas, population tuning appeared less organized (Fig. 9E). A statistical analysis of the distribution of preferred directions across the population of DS-RGCs confirmed greater disorder in S334ter-3 than WT retinas (Fig. 9F, $p = 0.0159$, *see Materials and Methods*,). However, Rao's spacing test of uniformity also indicated that the distribution of preferred directions was not random ($p < 0.05$), suggesting that some residual bias for the original cardinal axes persisted.

These results indicate that for individual and populations of DS-RGCs, rod death did not eliminate direction selectivity under photopic conditions. However, the reorganization of cones likely disrupted the direction tuning of individual cells and led to spurious direction tuning away from the cardinal axes (*see Discussion*). Note, ON DS-RGCs were not distinguished from ON-OFF DS-RGCs. However, nearly all (95%) recorded DS-RGCs exhibited OFF responses to decrements of light (data not shown) suggesting that most were ON-OFF DS-RGCs.

Spontaneous activity is elevated in many but not all types of RGCs

671 The spontaneous activity of RGCs defines the spiking activity upon which light-driven signals
672 must be detected (Barlow and Levick 1969; Copenhagen et al. 1987; Mastronarde 1983).
673 Increases in spontaneous activity generally signify a decreased signal-to-noise ratio for stimuli
674 near detection threshold. Therefore, to fully understand the functional consequences of rod death
675 on RGC signaling, it is necessary to determine the impact on spontaneous activity (Margolis and
676 Detwiler 2011; Stasheff 2008).
677
678 We found that the impact of rod death on the spontaneous activity of RGCs depended on cell
679 type. Spontaneous activity was measured using a static and uniform "gray" screen presented at a
680 photopic light level (*see Materials and Methods*). Most RGC types exhibited higher spontaneous
681 firing rates in S334ter-3 (Fig 10A and C), consistent with previous results (Dräger and Hubel
682 1978; Euler and Schubert 2015; Fransen et al. 2015; Stasheff 2008). On average, classified
683 RGCs exhibited a significant increase in spontaneous activity from 7.56 ± 0.79 Hz (n = 319) to
684 8.54 ± 0.33 Hz (n = 672, $p < 0.0001$, one-way Mann-Whitney test) and unclassified RGCs
685 exhibited an increase from 4.29 ± 0.30 Hz (n = 334) to 7.26 ± 0.27 Hz (n = 811, $p < 0.0001$, one-
686 way Mann-Whitney test). However, the fractional increase in spontaneous activity differed
687 between types (Fig 10C, $p = 0.006$ for OFF sluggish cells, and $p < 0.0001$ for all other types).
688 OFF brisk sustained RGCs, exhibited a twofold reduction in spontaneous activity (Fig. 10B,
689 raster plot, WT: 42.9 ± 1.7 Hz (n = 37), S334ter-3: 20.3 ± 0.7 Hz (n = 81), Fig. 10D, $p <$
690 0.0001). Therefore, in at least one RGC type, spontaneous activity decreases following rod death
691 and prior to cone death.
692

693 In addition to changes in the mean firing rate, photoreceptor death can induce oscillatory activity
694 among RGCs (Biswas et al. 2014; Borowska et al. 2011; Euler and Schubert 2015; Fransen et al.
695 2015; Margolis et al. 2014; Menzler and Zeck 2011; Stasheff 2008; Yee et al. 2012). This
696 oscillatory activity may also disrupt visual signaling. To determine whether different RGC types
697 exhibited increased oscillatory activity prior to cone death, a power spectral analysis of the
698 spontaneous activity was performed (Fig. 10E-H). This analysis revealed weak rhythmic activity
699 at ~7Hz among ON and OFF brisk sustained, OFF brisk transient, and ON small transient RGC
700 types in S334ter-3 but not WT retinas (Fig. 10E & F). This is weaker than, but generally
701 consistent with, oscillatory activity observed after the loss of both rods and cones (Borowska et
702 al. 2011; Yee et al. 2012). In other RGC types such as ON and OFF small transient cells, the
703 power spectral analysis revealed greater power at frequencies < 5 Hz than at higher frequencies
704 (Fig 10G-H). Thus, changes in both firing rates and the dominant spiking frequencies were RGC
705 type dependent.

706 # Discussion

707 Neural circuits throughout the brain are composed of many cell types. Learning how
708 degeneration of one type impacts other types in these circuits will provide a greater
709 understanding of the progression of these diseases and may point toward novel therapeutic
710 approaches. In this study, we measured the net effect of rod death on cone-mediated RFs and
711 light responses of many RGC types. We observed some changes that were ubiquitous across
712 RGC types and some changes that were cell-type dependent. Below, we comment on the
713 mechanisms that may underlie the observed changes in RFs and RGC physiology, we comment
714 on RGCs that were not functionally classified in this study, and we discuss some implications of
715 this study for treating RP.

RF changes: implications and potential mechanisms

RGC spatial RFs frequently exhibited arc-like shapes in S334ter-3 retinas (Fig. 7). These perturbations in the spatial RFs of individual cells also had consequences at the population level by disrupting the mosaic-like arrangement of RFs with homotypic neighbors (Fig. 4). These changes at both the single cell and population level can be explained largely, if not entirely by the reorganization of cones (Fig. 1 & 2). Functionally, the cone reorganization introduced blind-spots and locations with high cone density, which were reflected in the spatial RFs of the RGCs. We also observed a nearly linear relationship between the reduction in RF size in S334ter-3 retinas and RF size in WT retinas (Fig 7F): cell types with larger spatial RFs exhibited larger reductions in RF size in S334ter-3 animals. This can be explained by noting that the reorganization of cones decreases their nearest neighbor spacing, effectively decreasing the retinal area sampled by the cone mosaic. This manifests as a shrinking in the area sampled by the spatial RFs. Larger RFs sample from more cones and thus shrink more because they are subject to a decreased inter-cone spacing that propagates across more cones. Functionally, these changes in RF size increase the mean and decrease the range of spatial frequencies that strongly drive RGC spiking.

The mechanisms causing changes in the temporal RFs are less clear. While the temporal dynamics were slower for all RGCs in S334ter-3 retinas, the degree of change depended on type (Fig. 8). Thus, common and distinct mechanisms could be involved. A possible common mechanism is compromised cone health, which could slow their responses; rod death has been observed to compromise cone function by producing toxic byproducts and loss of trophic support

739 (Léveillard et al. 2004; Mohand-Said et al. 1997, 1998; Steinberg 1994). Another possible
740 common mechanism is a reduced cone collecting area for light, which would effectively dark-
741 adapt the cones; the response dynamics of cones are slower at lower light levels (Baylor et al.
742 1974, 1987). Cone outer segments were shorter and flattened in S334ter-3 retinas (Fig. 1; (Ji et
743 al. 2012)), which likely reduces their effective collecting area (Baylor and Fettiplace 1975;
744 Baylor and Hodgkin 1973; Sandberg et al. 1981). Rod death during retinal development may
745 also impact all retinal pathways (Cuenca et al. 2004, 2005; Martinez-Navarrete et al. 2011; Ray
746 et al. 2010; Strettoi et al. 2003). Rod loss can perturb postnatal maturation of cone pathways
747 (Banin et al. 1999), and light responses of RGCs are slower at the time of eye opening than in
748 adult rats (Anishchenko et al. 2010).
749
750 A possible pathway specific mechanism is differential changes in synaptic transmission between
751 cones and different cone bipolar cell types. Glutamate receptor expression on bipolar cells is
752 reduced and mislocalized with photoreceptor degeneration (Martinez-Navarrete et al. 2011;
753 Puthussery et al. 2009; Strettoi et al. 2003). This could generate a slower bipolar cell response
754 with differential effects among different bipolar cell types. Further experiments are needed to
755 distinguish between common and pathway specific mechanisms.
756
757 The spatiotemporal RFs of RGCs have also been examined in P23H-1 rats using approaches
758 similar to those used here to study S334ter-3 rats (i.e., checkerboard noise stimuli and MEA
759 recordings; Sekirnjak et al. 2011). Both P23H-1 and S334ter-3 rats have mutations in the gene
760 encoding for rhodopsin. In P23H-1, the mutation causes a misfolding of the protein; in S334ter-
761 3, the mutation results in a truncated C-terminus that likely leads to improper protein trafficking

(Liu et al. 1999; Martinez-Navarrete et al. 2011). P23H-1 animals exhibit a slower time course of rod photoreceptor death than S334ter-3, but both lines exhibit photoreceptor loss during development. Significant cone loss is observed before all rods have died in P23H-1 rats (Garcia-Ayuso et al. 2013); therefore, the two lines exhibit distinct dynamics in rod and cone death. Despite these differences, both lines exhibit rings of cones surrounding regions with few or no photoreceptors (Garcia-Ayuso et al. 2013; Ji et al. 2012). Average spatial RF size decreased and temporal integration increased in P23H-1 rats as photoreceptors died. These effects are qualitatively consistent with those reported here. However, the spatial RFs in P23H-1 rats were not reported to exhibit arc-like shapes. One possible explanation for this difference is that in those experiments, the spatial resolution of the RF measurements was 4 to 16-fold courser in area. This lower resolution could have blurred abnormal spatial RFs causing them to appear more Gaussian.

Mechanisms altering tuning of direction selective RGCs

Anatomical measurements indicate that DS-RGCs are ~15-20% of all RGCs in rat (Sun et al. 2002), consistent with the fraction RGCs identified as DS in this study. These cells receive input from precisely wired presynaptic circuits to respond selectively to motion direction regardless of stimulus polarity (Barlow and Hill 1963; Grzywacz and Amthor 1993; Lee et al. 2012; Trenholm et al. 2011). DS-RGCs are likely important for gaze stabilization, calibration of the vestibular system, and motion perception (Vaney et al. 2012). Therefore, understanding the impact of rod death on these cells is important for interpreting visual deficits measured behaviorally.

784 Rod death led to a broadening of DS tuning among individual RGCs and diminished the
785 population preferences for the cardinal axes (Fig. 9). One possible explanation for these
786 observations is that the reorganization of cones changed the direction and broadened the tuning
787 of individual DS-RGCs. A second possibility is that rod death caused a rewiring in the inner
788 retina that altered DS-RGC tuning. However, the extent of inner retinal remodeling is limited by
789 the observation that RGCs with direction selective responses were not eliminated by rod death; a
790 similar proportion of DS-RGCs were recorded in WT and S334ter-3 retinas. A third possible
791 explanation is that retinal development was altered by rod death. The fine-tuning of DS circuits
792 depends on visual experience (Bos et al. 2016; Chan and Chiao 2013; Chen et al. 2009; Elstrott
793 et al. 2008; Tian and Copenhagen 2003); thus, altered photoreceptor function may interrupt this
794 refinement. Further experiments are needed to determine the relative contributions of these
795 potential mechanisms.
796

797 ## Cell-type specific changes in spontaneous activity

798 Spontaneous spiking activity sets a baseline noise level against which signals near threshold
799 must compete (Barlow and Levick 1969; Troy 1983). Changes in spontaneous activity can
800 therefore strongly impact behavior and perception (Aho et al. 1988). We observed changes in
801 spontaneous activity following rod death that were RGC-type specific. Given that each RGC
802 type signals different visual features to the brain, cell-type dependent changes in spontaneous
803 activity predict that some visually guided behaviors may be more severely impacted by rod death
804 than others. Further work to understand the relationship between different RGC types and
805 behaviors in rodents (Yilmaz and Meister 2013; Yoshida et al. 2001) is needed to test rigorously
806 this prediction.

807

808 Changes in spontaneous activity have been observed and studied in many animal models of RP
809 (Choi et al. 2014; Dräger and Hubel 1978; Fransen et al. 2015; Margolis et al. 2008, 2014;
810 Menzler and Zeck 2011; Pu et al. 2006; Sekirnjak et al. 2011; Stasheff 2008; Stasheff et al. 2011;
811 Toychiev et al. 2013). Recent work has also indicated that these changes depend on RGC type
812 (Sekirnjak et al. 2011; Yee et al. 2012, 2014). However, there are several differences between
813 previous studies and the experiments described here. Previous studies primarily classified RGCs
814 according to morphological features or simple functional distinctions (e.g., ON vs OFF), and
815 these classifications were not validated by checking whether cells of a given type exhibited a
816 mosaic organization (Sekirnjak et al. 2011; Yee et al. 2012, 2014). Furthermore, these studies
817 largely (but not exclusively) focused on time points after which all photoreceptors were lost. Our
818 study provides a distinct yet complementary view. First, RGCs were classified functionally
819 rather than morphologically. Second, large-scale MEA recordings allowed us to validate the
820 classification by testing for a mosaic organization within each RGC type. Third, we focused
821 exclusively on a time point at which the vast majority of rods were dead (99.99%), but cones
822 persisted. We found that most RGC types exhibited elevated spontaneous activity, but the
823 increase depended on cell type (Fig. 10A and C). Furthermore, OFF brisk sustained RGCs
824 exhibited a substantial reduction in spontaneous activity (Fig. 10B and D).

825

826 The spontaneous activity of RGCs has been measured in P23H-1 rats (Fransen et al. 2015;
827 Sekirnjak et al. 2011). OFF RGCs, but not ON, exhibited elevated spontaneous activity in that
828 model. This effect on spontaneous activity is distinct from that observed here and reported in rd1
829 and rd10 mice (Margolis et al. 2014; Stasheff 2008; Stasheff et al. 2011; Yee et al. 2012). This

suggests that different causes and trajectories toward photoreceptor loss can have different effects on retinal circuits and RGC function.

Oscillatory activity has also been noted in many animal models of RP (Borowska et al. 2011; Haq et al. 2014; Margolis et al. 2008; Menzler et al. 2014; Yee et al. 2014). Low frequency oscillations (~1 Hz) appear to be driven by horizontal cells (Haq et al. 2014), while higher frequency oscillations (~7-14 Hz) appear to be driven by either a coupled network of ON cone bipolar cells and AII amacrine cells or by AII amacrine cells alone (Borowska et al. 2011; Choi et al. 2014; Euler and Schubert 2015; Margolis et al. 2014; Yee et al. 2012). The results presented here indicate that the higher frequency oscillations appear prior to cone death in S334ter-3 rats, but not in all RGC types. This may result from some RGC types receiving stronger direct or indirect input from the network of AII amacrine cells. Further experiments are needed to determine whether lower frequency oscillations may become more substantial at later stages of degeneration.

Unclassified RGCs

In WT and S334ter-3 experiments, ~40% of recorded RGCs were successfully classified. The rodent retina contains 30-40 RGC types (Baden et al. 2016; Sanes and Masland 2015; Sümbül et al. 2014), and we distinguished just 11 types. Our limited ability to classify these remaining cells largely stemmed from recording from too few cells of a given type in a single experiment to reveal a mosaic arrangement of RGCs. Without this verification step, it is difficult to accurately make cell-type specific comparisons between control and disease conditions, which was the main objective of this study.

The trends of slower temporal RFs and irregularly shaped spatial RFs observed among classified RGCs were also observed among unclassified cells. However, because this comparison is not cell-type specific, we cannot rule out the possibility that some RGC types exhibit opposite trends. Further technical developments to improve large-scale neural population recordings will likely allow for more complete cell-type specific comparisons between healthy and disease retinas. For example, more sophisticated spike-sorting algorithms (Marre et al. 2012; Prentice et al. 2011) may increase the number of identified neurons. More identified neurons may provide sufficient statistical power to classify more cell types. Cell yield may also be increased by using denser electrode arrays or Ca^{2+} imaging of neural activity (Baden et al. 2016). It is also possible that using additional visual stimuli would aid the identification of more RGC types. For example, some rodent RGC types exhibit strong surround suppression such that they only respond to stimuli localized to their RF center (Jacoby and Schwartz 2017; Zhang et al. 2012). These cells would be expected to respond poorly to full-field checkerboard noise and the drifting gratings used in this study. Therefore, developing more refined stimuli, recording technologies and spike sorting procedures, will ultimately allow a more complete and cell-type specific view of retinal degeneration.

Implications for RP

RP results from one of many possible gene mutations and leads to severe vision loss in humans (Bowes et al. 1990; Farber and Lolley 1974; Marc and Jones 2003; Rosenfeld et al. 1992). Regardless of the underlying genetic defect, the disease begins with the degeneration of rod

875 photoreceptors followed by the degeneration of cones and an eventual rewiring of the remaining
876 retinal neurons (Jones et al. 2003; Jones and Marc 2005; Strettoi 2015).
877
878 To study the impact of rod death on retinal signaling prior to the death of cones, we used
879 S334ter-3 rats. Disease progression in this animal model has at least two important differences
880 from disease progression in humans. First, rods begin to die rapidly in S334ter-3 animals prior to
881 the end of retinal development, similar to rd1 mice (Stasheff et al. 2011). Thus, the results
882 presented here may be partly caused by altered retinal development. Second, rod death in
883 S334ter-3 rats is temporally distinct from cone death and results in a reorganization of the cone
884 mosaic (Figs. 1 & 2). It is unclear whether cones are reorganized in a similar fashion in any
885 human forms of RP (Makiyama et al. 2013; Park et al. 2014). However, the existence of cone
886 rings has been reported in human retinal dystrophies, inherited retinal degeneration, and photo-
887 pigment genetic perturbations in M-opsin cones (Carroll et al. 2004; Choi et al. 2006; Duncan et
888 al. 2007; Rossi et al. 2011). Thus, cone rings are a pathologic hallmark of many retinal
889 dystrophies. We therefore view this animal model as one tool among many to understand the
890 impact of RP (and potentially other diseases) on retinal function. The advantages of this animal
891 model are that it (1) provides a temporal window to probe cone-mediated responses following
892 rod death, and that it (2) exhibits an extensive and clear remodeling in the outer retina the
893 consequences of which can be measured across diverse RGC types.
894
895 Determining when photoreceptor death causes substantial rewiring of retinal circuits will likely
896 inform therapeutic strategies for restoring vision. After all photoreceptors are lost, the retina
897 eventually undergoes a profound remodeling (Jones et al. 2003, 2016). It is less clear the extent

898 to which the retina changes prior to the loss of all photoreceptors. Anatomical studies have
899 provided conflicting data about the timescale at which cell death in the outer retina propagates to
900 changes in the morphology of RGCs and other cells in the inner retina (Jones et al. 2011;
901 Martinez-Navarrete et al. 2011; Ray et al. 2010; Strettoi et al. 2002, Mazzoni et al. 2008). An
902 underlying goal of these studies is to determine the extent to which retinal circuitry is stable in
903 the face of rod death. However, it is difficult to predict how anatomical stability (or lack thereof)
904 corresponds to functional stability. Subtle anatomical changes could have substantial functional
905 consequences. Alternatively, function could be relatively stable despite a structural
906 reorganization (Margolis et al. 2008; Yee et al. 2012). We used large-scale parallel recordings of
907 RGC function to determine the impact of rod photoreceptor death on the output neurons of the
908 retina prior to cone death. One important observation was that functionally distinct RGC types
909 persisted (Fig 3). The retention of functionally distinct RGCs following rod death lends support
910 to the idea that rod photoreceptor replacement may largely restore vision (Acland et al. 2001;
911 Bakondi et al. 2016; Bennett et al. 2012; MacLaren et al. 2006; Tucker et al. 2011). This
912 retention of RGC types is also consistent with the idea that during the period of rod death, viral-
913 mediated gene-therapy approaches to restore rod function may be highly successful at halting
914 retinal degeneration and vision loss (Acland et al. 2001; Ali et al. 2000; Pierce and Bennett
915 2015).
916
917 While the persistence of functionally distinct RGCs following rod death is promising, the altered
918 spatiotemporal RFs and spontaneous activity of RGCs under cone-mediated signaling conditions
919 presents a potential challenge to restoring normal vision (Figs. 7-10). For example, human RP
920 patients have diminished temporal resolution of vision prior to the loss of cones (Alexander et al.

921 2003; Dagnelie and Massof 1993), consistent with our observation of prolonged temporal
922 integration within the RFs of RGCs. It is unclear whether simply replacing lost rods will restore
923 this aspect of cone-mediated vision. Secondary therapies may be required to counteract changes
924 in retinal circuits that change the spatiotemporal RFs and spontaneous activity of RGCs (Euler
925 and Schubert 2015). This points to the importance of understanding fully the changes in retinal
926 function induced by rod death and determining the cellular mechanisms that drive these changes.
927

Figure Captions

Figure 1. Remodeling of the cone mosaic in S334ter-3 RP rats at P60. A & B. Confocal micrographs of vertical sections showing M-opsin immunoreactivity in WT **(A)** and S334ter-3 **(B)** retinas. Cone outer segments are shorter and distorted (**B,** arrows). Scale bar, 10 μm. **C & D.** M-opsin immunoreactivity from confocal micrographs of whole-mount retinas in WT **(C)** and S334ter-3 **(D)** rats. Homogeneous distributions of M-opsin containing cones in WT retina; cones are organized into rings in S334ter-3 retina. Scale bars, 100 μm.

Figure 2. Functional changes in spatial sensitivity in S334ter-3 retina. A. Spatial RFs of two ON and two OFF RGCs from WT retina. Red (blue) indicates sensitivity to increments (decrements) of light. **B.** Spatial RFs from S334ter-3 retina. RFs exhibit holes and arc-like shapes. Scale bar, 150 μm. **C.** Binary map indicating locations of high (whites) versus low (black) sensitivity to light cumulated across all recorded RGCs for a WT rat. **D.** Same as **C** for S334ter-3 retina. Inset: micrograph shows the outer segments of cones from S334ter-3 retina at same scale as sensitivity map. Red hexagon is MEA border. Scale bar, 100 μm.

Figure 3. Functional classification of RGCs in WT and S334ter-3 retinas. A. Identification of DS-RGCs in one WT retina (WT3 in Table 1). Scatter plot of vector sums to a high and a low speed drifting gratings for all RGCs in one recording (Gratings 1 & 2, spatial periods: 512 μm, temporal periods 0.5 s & 2.0 s). Colored points show results of a two-Gaussian mixture model fit. Red points are DS-RGCs. **B.** Classification of ON brisk sustained RGCs. Scatter plot of

indicated response parameters measured from all ON RGCs. Colored points show results of a two-Gaussian mixture model fit. Red points are identified ON brisk sustained RGCs. **C.** Scatter plot showing all ON RGCs with ON brisk sustained cells removed. Colored points show results of a two-Gaussian mixture model fit to points; red points are identified ON brisk transient (BT) RGCs. **D.** Scatter plot of remaining ON RGCs in the indicated parameter space. Colored points show the results of a two-Gaussian mixture model fit with red points identifying the ON small transient RGCs. **E-H.** Same as A-D but shows results of classification of each RGC type from one S334ter-3 recording (RP1 in Table 1). **I-L.** Result of serial classification for OFF brisk sustained, OFF brisk transient, OFF small transient, and OFF sluggish RGCs. **I** shows all OFF cells, **J** shows all OFF cells with OFF BS cells removed, **K** shows all OFF cells with OFF BS and BT removed, **L** shows all OFF cells with OFF BS, BT, and ST removed. Colored points show the results of a two-Gaussian mixture model fit; red points indicate the classified cells in each panel. **M-P.** Same as **I-L**, but for the S334ter-3 recording in **E-H.** TC: time course of temporal RF; PC: principal components; ISI: inter-spike interval histogram.

Figure 4. RGCs exhibited regular spacing within identified types in WT and S334ter-3 retinas. A. *Top left:* RF contours for ON Small Transient RGCs in one WT retina recording. Contours drawn at 60% of RF peak. Hexagon indicates outline of electrode array. *Top right:* RGC locations estimated from electrical image of each cell. Only cells with locations well estimated by the electrical image are plotted. *Bottom:* Histogram of nearest neighbor distances cumulated over 4 recordings. Magenta curve is nearest neighbor distribution of randomly sampled RGC locations (across all RGC types) measured across recordings. Shaded area is SD. **B**. Same as **A,** but for ON Small Transient RGCs identified in S334ter-3 retina. RF contours

(panel **B**, *top left*) drawn at 40% of peak RF and distinctly colored to aid in the visualization of their shapes. **C & D, E & F, G & H.** Same as **A** and **B**, but for ON Brisk Transient, OFF Brisk Sustained and OFF Brisk Transient RGCs, respectively from WT and S334ter-3 recordings. RF contours drawn at 60% of peak for all WT data (**A**, **C**, **E**, **& G**) and at 40% for all RP data (**B**, **D**, **F**, **& H**). MEA is 450 μm across from the left and right hexagon corners.

Figure 5. Temporal RFs and full-field light steps match RGC types between WT and S334ter-3 retinas. A & B. Mean temporal RFs of 3 ON RGC types from all WT and S334ter-3 retinas, respectively. **C & D.** Mean temporal RFs of 4 OFF RGC types from all WT and S334ter-3 retina, respectively. Lines are average time courses. Shaded regions show 1-SD. RGC types were matched between WT and S334ter-3 recordings by a minimum matching algorithm RFs (*see Materials and Methods)* **E.** Comparison of PSTHs from 3 ON and 4 OFF RGC types identified from WT and S334ter-3 retinas. RGC types were matched by applying a minimum matching algorithm to the PSTHs. Staircase on far right indicates time course of the stimulus which started at "white" then transitioned through "gray", "black" and back to "gray," switching intensity every 3 s. RP indicates data from S334ter-3 retinas.

Figure 6. Spike waveforms match RGC types between WT and S334ter-3 retinas. A & B. Mean spike waveforms from three ON RGC types in WT (**A**) and S334ter-3 (**B**) retinas. Solid lines are mean and shaded areas are the SD. Spike waveforms exhibit type-dependent differences in dynamics. **C.** Mean spike waveforms for ON brisk sustained (red), brisk transient (blue), and small transient (green) RGCs are plotted in a two-dimensional subspace defined by PCA applied to the spike waveforms across retinas. Each symbol is the mean spike waveform for a cell type

997 from a different recording, filled symbols are from S344ter-3 retinas. **D & E.** Mean and SD of
998 spike waveforms for four OFF RGC types from WT (**D**) and S334ter-3 (**E**). **F.** OFF brisk
999 sustained (red), brisk transient (blue), small transient (green) and sluggish (magenta) RGC types
1000 are plotted in a three-dimensional subspace defined by PCA. Ellipses show 1.3-sigma contours
1001 of three-dimensional Gaussian fits to each group of points. **Inset.** Two-dimensional subspace
1002 defined by PCA applied to spike shapes for just three OFF RGC types yields similar clustering as
1003 that observed for the three ON RGC types (**C**).
1004
1005 **Figure 7. Impact of RP on the spatial RFs of distinct RGC types. A.** Representative spatial
1006 RFs for OFF brisk transient (BT), OFF sluggish, and ON small transient (ON ST) RGCs in WT
1007 (top) and S334ter-3 (bottom) retinas. **B.** Illustration of data processing for computation of the
1008 convexity index (*top,* CI). Probability density of convexity index for 3 ON, 3 OFF, and
1009 unclassified RGCs types from WT (black) and S334ter3 (green, RP) retinas (bottom). **C, D.**
1010 Correlation between convexity index and RF displacement in WT (R^2 = 0.002, β = -33.6, p =
1011 0.4947) and S334ter-3 (R^2 = 0.23, β = -141.4, $p < 0.00001$) retinas. **E.** Reduction of RF sizes in
1012 S334ter-3 retinas ($p < 0.0002$ for all the types). Error bars are SE. **F.** Linear relationship between
1013 spatial RF sizes estimated in WT retinas and observed size reduction in S334ter-3 retinas. Each
1014 point shows a different RGC type from **E**.
1015
1016 **Figure 8. Changes in RGC temporal integration in S334ter-3 retinas. A.** Comparison of
1017 temporal RFs for 3 ON and 4 OFF RGC types in WT (black) and S334ter-3 (green) retinas.
1018 Lines indicate mean values, shaded areas show SE. Scale bar is 100 ms. Right corner panel:
1019 illustration of extracted quantities from temporal RFs: time-to-first-peak preceding spike (a),

time-to-zero-crossing (b), degree of transiency (DoT, S1 and S2 are areas under the curve). **B, C, D.** Comparison of time-to-first-peak ($p < 0.0001$ for all the types) **(B)**, time-to-zero-crossing **(C)**, and degree of transiency **(D)** between WT and S334ter-3 retinas for 7 RGC types. Points show mean and SE.

Figure 9. Direction tuning preferences are disrupted among DS-RGCs in S334ter-3 retina. **A.** Direction tuning for a DS-RGCs from an S334ter-3 retina. Dots show average firing rates and gray curve is a fitted von Mises function. **B.** Distribution of tuning widths at half height for DS-RGCs in WT (black) and S334ter-3 (green) retinas. **C.** Skewness distribution of tuning curves for DS-RGCs in WT (black) and S334ter-3 (green) retinas. **D, E.** Directional preferences of DS cells in one WT (**D**) and one S334ter-3 (**E**) retina. **F.** Homogeneity test for the distribution of preferred directions (mean and SE).

Figure 10. Changes in spontaneous activity in S334ter-3 retinas are RGC type dependent. **A.** Spontaneous firing for ON brisk sustained RGCs from WT and S334ter-3 retinas. Each row shows spike times for a different RGC recorded simultaneously (scale bar: 500 ms). Array outlines (hexagons) show estimated soma locations of recorded RGCs (black points) and lines point to corresponding row of the raster. **B.** Identical to **A**, but for OFF brisk sustained RGCs. **C.** Mean spontaneous firing rates for seven types of ganglion cells (mean ± SE) **D.** Mean spontaneous firing rates for OFF brisk sustained RGCs (mean ± SE). **E & F.** Power spectra of the spontaneous spiking for ON brisk sustained RGCs (**E**) and OFF brisk sustained RGCs (**F**) from WT and S334ter-3 (RP) retinas. **G & H.** Power spectra of the spontaneous spiking for ON and OFF small transient RGCs from WT and S334ter-3 retinas.

1043

Table 1

Group	Total	DS	ON Sus	ON LT	ON ST	OFF Sus	OFF LT	OFF ST	OFF Sluggish
WT 1	252	44	4	15	5	9	14	8	0
WT 2	238	44	10	10	8	6	7	7	11
WT 3	317	51	15	18	14	13	16	12	5
WT 4	356	62	13	19	12	10	14	15	0
RP 1	369	54	16	21	16	15	22	6	14
RP 2	411	63	23	15	7	27	24	2	0
RP 3	309	50	13	6	13	13	11	9	10
RP 4	341	59	12	17	11	13	13	12	21
RP 5	324	37	8	23	14	13	10	13	14

Table 1. Number of cells identified for each RGC type in 4 WT and 5 S334ter-3 RP retinas. Total number of recorded RGCs (classified + unclassified) is 1163 and 1754 in WT and RP respectively. The percentage of cells identified in each RGC type was not significantly different between WT and S334ter-3 except for OFF sluggish cells (1.5 ± 1.1% and 3.5 ± 1.0%, $p = 0.003$, WT and S334ter-3, respectively).

Bibliography

Acland GM, Aguirre GD, Ray J, Zhang Q, Aleman TS, Cideciyan AV, Pearce-Kelling SE, Anand V, Zeng Y, Maguire AM. Gene therapy restores vision in a canine model of childhood blindness. *Nature genetics* 28: 92-95, 2001.

Aho AC, Donner K, Hyden C, Larsen LO, Reuter T. Low retinal noise in animals with low body temperature allows high visual sensitivity. *Nature* 334: 348-350, 1988.

Alexander KR, Barnes CS, Fishman GA. Deficits in temporal integration for contrast processing in retinitis pigmentosa. *Invest Ophthalmol Vis Sci* 44: 3163-3169, 2003.

Ali RR, Sarra GM, Stephens C, Alwis MD, Bainbridge JW, Munro PM, Fauser S, Reichel MB, Kinnon C, Hunt DM, Bhattacharya SS, Thrasher AJ. Restoration of photoreceptor ultrastructure and function in retinal degeneration slow mice by gene therapy. *Nat Genet* 25: 306-310, 2000.

Amthor FR, Takahashi ES, Oyster CW. Morphologies of rabbit retinal ganglion cells with complex receptive fields. *J Comp Neurol* 280: 97-121, 1989a.

Amthor FR, Takahashi ES, Oyster CW. Morphologies of rabbit retinal ganglion cells with concentric receptive fields. *J Comp Neurol* 280: 72-96, 1989b.

Anishchenko A, Greschner M, Elstrott J, Sher A, Litke AM, Feller MB, Chichilnisky EJ. Receptive field mosaics of retinal ganglion cells are established without visual experience. *J Neurophysiol* 103: 1856, 2010.

Baden T, Berens P, Franke K, Román Rosón M, Bethge M, Euler T. The functional diversity of retinal ganglion cells in the mouse. *Nature* 529: 345-350, 2016.

Bakondi B, Lv W, Lu B, Jones MK, Tsai Y, Kim KJ, Levy R, Akhtar AA, Breunig JJ, Svendsen CN, Wang S. In Vivo CRISPR/Cas9 Gene Editing Corrects Retinal Dystrophy in the S334ter-3 Rat Model of Autosomal Dominant Retinitis Pigmentosa. *Mol Ther* 24: 556-563, 2016.

Banin E, Cideciyan AV, Alemán TS, Petters RM, Wong F, Milam AH, Jacobson SG. Retinal rod photoreceptor-specific gene mutation perturbs cone pathway development. *Neuron* 23: 549-557, 1999.

Barlow HB, Hill RM. Selective sensitivity to direction of movement in ganglion cells of the rabbit retina. *Science* 139: 412-414, 1963.

Barlow HB, Levick WR. Changes in the maintained discharge with adaptation level in the cat retina. *J Physiol* 202: 699-718, 1969.

Baylor DA, Fettiplace R. Light path and photon capture in turtle photoreceptors. *J Physiol* 248: 433-464, 1975.

Baylor DA, Hodgkin AL. Detection and resolution of visual stimuli by turtle photoreceptors. *J Physiol* 234: 163-198, 1973.

Baylor DA, Hodgkin AL, Lamb TD. The electrical response of turtle cones to flashes and steps of light. *J Physiol (Lond)* 242: 685-727, 1974.

Baylor DA, Nunn BJ, Schnapf JL. The photocurrent, noise and spectral sensitivity of rods of the monkey Macaca fascicularis. *J Physiol* 357: 575-607, 1984.

Baylor DA, Nunn BJ, Schnapf JL. Spectral sensitivity of cones of the monkey Macaca fascicularis. *J Physiol* 390: 145-160, 1987.

Bennett J, Ashtari M, Wellman J, Marshall KA, Cyckowski LL, Chung DC, McCague S, Pierce EA, Chen Y, Bennicelli JL. AAV2 gene therapy readministration in three adults with congenital blindness. *Science translational medicine* 4: 120ra15-120ra15, 2012.

Berens P. CircStat: a MATLAB toolbox for circular statistics. *J Stat Softw* 31: 1-21, 2009.

Biswas S, Haselier C, Mataruga A, Thumann G, Walter P, Müller F. Pharmacological analysis of intrinsic neuronal oscillations in rd10 retina. *PLoS One* 9: e99075, 2014.

Borowska J, Trenholm S, Awatramani GB. An intrinsic neural oscillator in the degenerating mouse retina. *J Neurosci* 31: 5000-5012, 2011.

Bos R, Gainer C, Feller MB. Role for Visual Experience in the Development of Direction-Selective Circuits. *Curr Biol* 26: 1367-1375, 2016.

Bowes C, Li T, Danciger M, Baxter LC, Applebury ML, Farber DB. Retinal degeneration in the rd mouse is caused by a defect in the subunit of rod cGMP-phosphodiesterase. *Nature* 347: 677-680, 1990.

Briggman KL, Helmstaedter M, Denk W. Wiring specificity in the direction-selectivity circuit of the retina. *Nature* 471: 183-188, 2011.

Caldwell JH, Daw NW. New properties of rabbit retinal ganglion cells. *J Physiol* 276: 257-276, 1978.

Cao Y, Sarria I, Fehlhaber KE, Kamasawa N, Orlandi C, James KN, Hazen JL, Gardner MR, Farzan M, Lee A, Baker S, Baldwin K, Sampath AP, Martemyanov KA. Mechanism

for Selective Synaptic Wiring of Rod Photoreceptors into the Retinal Circuitry and Its Role in Vision. *Neuron* 87: 1248-1260, 2015.

Carroll J, Neitz M, Hofer H, Neitz J, Williams DR. Functional photoreceptor loss revealed with adaptive optics: an alternate cause of color blindness. *Proc Natl Acad Sci U S A* 101: 8461-8466, 2004.

Chan LL, Lee EJ, Humayun MS, Weiland JD. Both electrical stimulation thresholds and SMI-32-immunoreactive retinal ganglion cell density correlate with age in S334ter line 3 rat retina. *J Neurophysiol* 105: 2687-2697, 2011.

Chan YC, Chiao CC. The distribution of the preferred directions of the ON-OFF direction selective ganglion cells in the rabbit retina requires refinement after eye opening. *Physiol Rep* 1: e00013, 2013.

Chen K, Wang Y, Liang X, Zhang Y, Ng TK, Chan LL. Electrophysiology Alterations in Primary Visual Cortex Neurons of Retinal Degeneration (S334ter-line-3) Rats. *Sci Rep* 6: 26793, 2016.

Chen M, Weng S, Deng Q, Xu Z, He S. Physiological properties of direction-selective ganglion cells in early postnatal and adult mouse retina. *J Physiol* 587: 819-828, 2009.

Chichilnisky EJ. A simple white noise analysis of neuronal light responses. *Network: Computation in Neural Systems* 12: 199-213, 2001.

Chichilnisky EJ, Kalmar RS. Functional asymmetries in ON and OFF ganglion cells of primate retina. *J Neurosci* 22: 2737-2747, 2002.

Choi H, Zhang L, Cembrowski MS, Sabottke CF, Markowitz AL, Butts DA, Kath WL, Singer JH, Riecke H. Intrinsic bursting of AII amacrine cells underlies oscillations in the rd1 mouse retina. *J Neurophysiol* 112: 1491-1504, 2014.

Choi SS, Doble N, Hardy JL, Jones SM, Keltner JL, Olivier SS, Werner JS. In vivo imaging of the photoreceptor mosaic in retinal dystrophies and correlations with visual function. *Invest Ophthalmol Vis Sci* 47: 2080-2092, 2006.

Cleland BG, Levick WR. Properties of rarely encountered types of ganglion cells in the cat's retina and an overall classification. *J Physiol* 240: 457-492, 1974.

Cleland BG, Levick WR, Sanderson KJ. Properties of sustained and transient ganglion cells in the cat retina. *J Physiol* 228: 649-680, 1973.

Copenhagen DR, Donner K, Reuter T. Ganglion cell performance at absolute threshold in toad retina: effects of dark events in rods. *J Physiol* 393: 667-680, 1987.

Cruz-Martín A, El-Danaf RN, Osakada F, Sriram B, Dhande OS, Nguyen PL, Callaway EM, Ghosh A, Huberman AD. A dedicated circuit links direction-selective retinal ganglion cells to the primary visual cortex. *Nature* 507: 358-361, 2014.

Cuenca N, Pinilla I, Sauve Y, Lu B, Wang S, Lund RD. Regressive and reactive changes in the connectivity patterns of rod and cone pathways of P23H transgenic rat retina. *Neuroscience* 127: 301-317, 2004.

Cuenca N, Pinilla I, Sauve Y, Lund R. Early changes in synaptic connectivity following progressive photoreceptor degeneration in RCS rats. *Eur J Neurosci* 22: 1057-1072, 2005.

Dacey DM. The mosaic of midget ganglion cells in the human retina. *J Neurosci* 13: 5334-5355, 1993.

Dagnelie G, Massof RW. Foveal cone involvement in retinitis pigmentosa progression assessed through psychophysical impulse response parameters. *Investigative ophthalmology & visual science* 34: 243-255, 1993.

Della Santina L, Inman DM, Lupien CB, Horner PJ, Wong RO. Differential progression of structural and functional alterations in distinct retinal ganglion cell types in a mouse model of glaucoma. *J Neurosci* 33: 17444-17457, 2013.

Demb JB. Cellular mechanisms for direction selectivity in the retina. *Neuron* 55: 179-186, 2007.

Devries SH, Baylor DA. Mosaic arrangement of ganglion cell receptive fields in rabbit retina. *J Neurophysiol* 78: 2048-2060, 1997.

Ding H, Smith RG, Poleg-Polsky A, Diamond JS, Briggman KL. Species-specific wiring for direction selectivity in the mammalian retina. *Nature* 535: 105-110, 2016.

Dräger UC, Hubel DH. Studies of visual function and its decay in mice with hereditary retinal degeneration. *J Comp Neurol* 180: 85-114, 1978.

Duncan JL, Zhang Y, Gandhi J, Nakanishi C, Othman M, Branham KE, Swaroop A, Roorda A. High-resolution imaging with adaptive optics in patients with inherited retinal degeneration. *Invest Ophthalmol Vis Sci* 48: 3283-3291, 2007.

Dunn FA. Photoreceptor ablation initiates the immediate loss of glutamate receptors in postsynaptic bipolar cells in retina. *J Neurosci* 35: 2423-2431, 2015.

Elstrott J, Anishchenko A, Greschner M, Sher A, Litke AM, Chichilnisky EJ, Feller MB. Direction selectivity in the retina is established independent of visual experience and cholinergic retinal waves. *Neuron* 58: 499-506, 2008.

Euler T, Schubert T. Multiple Independent Oscillatory Networks in the Degenerating Retina. *Front Cell Neurosci* 9: 444, 2015.

Farber DB, Lolley RN. Cyclic guanosine monophosphate: elevation in degenerating photoreceptor cells of the C3H mouse retina. *Science* 186: 449-451, 1974.

Field GD, Chichilnisky EJ. Information processing in the primate retina: circuitry and coding. *Annu Rev Neurosci* 30: 1-30, 2007.

Field GD, Gauthier JL, Sher A, Greschner M, Machado TA, Jepson LH, Shlens J, Gunning DE, Mathieson K, Dabrowski W, Paninski L, Litke AM, Chichilnisky EJ. Functional connectivity in the retina at the resolution of photoreceptors. *Nature* 467: 673-677, 2010.

Field GD, Greschner M, Gauthier JL, Rangel C, Shlens J, Sher A, Marshak DW, Litke AM, Chichilnisky EJ. High-sensitivity rod photoreceptor input to the blue-yellow color opponent pathway in macaque retina. *Nat Neurosci* 12: 1159-1164, 2009.

Field GD, Rieke F. Mechanisms regulating variability of the single photon responses of mammalian rod photoreceptors. *Neuron* 35: 733-747, 2002.

Field GD, Sher A, Gauthier JL, Greschner M, Shlens J, Litke AM, Chichilnisky EJ. Spatial properties and functional organization of small bistratified ganglion cells in primate retina. *J Neurosci* 27: 13261-13272, 2007.

Fransen JW, Pangeni G, Pyle IS, McCall MA. Functional changes in Tg P23H-1 rat retinal responses: differences between ON and OFF pathway transmission to the superior colliculus. *J Neurophysiol* 114: 2368-2375, 2015.

Garcia-Ayuso D, Ortin-Martinez A, Jiménez-López M, Galindo-Romero C, Cuenca N, Pinilla I, Vidal-Sanz M, Agudo-Barriuso M, Villegas-Pérez MAP. Changes in the photoreceptor mosaic of P23H-1 rats during retinal degeneration: implications for rod-cone dependent survival. *Invest Ophthalmol Vis Sci* 54: 5888-5900, 2013.

Gargini C, Terzibasi E, Mazzoni F, Strettoi E. Retinal organization in the retinal degeneration 10 (rd10) mutant mouse: a morphological and ERG study. *J Comp Neurol* 500: 222-238, 2007.

Gauthier JL, Field GD, Sher A, Greschner M, Shlens J, Litke AM, Chichilnisky EJ. Receptive fields in primate retina are coordinated to sample visual space more uniformly. *PLoS Biol* 7: e63, 2009.

Grzywacz NORBERTOM, Amthor FRANKLINR. Facilitation in ON-OFF directionally selective ganglion cells of the rabbit retina. *Journal of Neurophysiology* 69: 2188-2199, 1993.

Grzywacz NM, Yuille AL. Massively parallel implementations of theories for apparent motion. *Spatial Vision* 3: 15-44, 1988.

Hammond P. Cat retinal ganglion cells: size and shape of receptive field centres. *J Physiol* 242: 99-118, 1974.

Haq W, Arango-Gonzalez B, Zrenner E, Euler T, Schubert T. Synaptic remodeling generates synchronous oscillations in the degenerated outer mouse retina. *Front Neural Circuits* 8: 108, 2014.

Heine WF, Passaglia CL. Spatial receptive field properties of rat retinal ganglion cells. *Visual neuroscience* 28: 403-417, 2011.

Hoggarth A, McLaughlin AJ, Ronellenfitch K, Trenholm S, Vasandani R, Sethuramanujam S, Schwab D, Briggman KL, Awatramani GB. Specific wiring of distinct amacrine cells in the directionally selective retinal circuit permits independent coding of direction and size. *Neuron* 86: 276-291, 2015.

Jacoby J, Schwartz GW. Three Small-Receptive-Field Ganglion Cells in the Mouse Retina Are Distinctly Tuned to Size, Speed, and Object Motion. *J Neurosci* 37: 610-625, 2017.

Ji Y, Zhu CL, Grzywacz NM, Lee EJ. Rearrangement of the cone mosaic in the retina of the rat model of retinitis pigmentosa. *J Comp Neurol* 520: 874-888, 2012.

Jones BW, Kondo M, Terasaki H, Watt CB, Rapp K, Anderson J, Lin Y, Shaw MV, Yang JH, Marc RE. Retinal remodeling in the Tg P347L rabbit, a large-eye model of retinal degeneration. *J Comp Neurol* 519: 2713-2733, 2011.

Jones BW, Marc RE. Retinal remodeling during retinal degeneration. *Exp Eye Res* 81: 123-137, 2005.

Jones BW, Pfeiffer RL, Ferrell WD, Watt CB, Marmor M, Marc RE. Retinal remodeling in human retinitis pigmentosa. *Exp Eye Res* 2016.

Jones BW, Watt CB, Frederick JM, Baehr W, Chen CK, Levine EM, Milam AH, Lavail MM, Marc RE. Retinal remodeling triggered by photoreceptor degenerations. *J Comp Neurol* 464: 1-16, 2003.

Krishnamoorthy V, Cherukuri P, Poria D, Goel M, Dagar S, Dhingra NK. Retinal Remodeling: Concerns, Emerging Remedies and Future Prospects. *Front Cell Neurosci* 10: 38, 2016.

Lee DC, Vazquez-Chona FR, Ferrell WD, Tam BM, Jones BW, Marc RE, Moritz OL. Dysmorphic photoreceptors in a P23H mutant rhodopsin model of retinitis pigmentosa are metabolically active and capable of regenerating to reverse retinal degeneration. *J Neurosci* 32: 2121-2128, 2012.

Lee EJ, Ji Y, Zhu CL, Grzywacz NM. Role of Müller cells in cone mosaic rearrangement in a rat model of retinitis pigmentosa. *Glia* 59: 1107-1117, 2011.

Léveillard T, Mohand-Saïd S, Lorentz O, Hicks D, Fintz AC, Clérin E, Simonutti M, Forster V, Cavusoglu N, Chalmel F, Dollé P, Poch O, Lambrou G, Sahel JA. Identification and characterization of rod-derived cone viability factor. *Nat Genet* 36: 755-759, 2004.

Li PH, Gauthier JL, Schiff M, Sher A, Ahn D, Field GD, Greschner M, Callaway EM, Litke AM, Chichilnisky EJ. Anatomical identification of extracellularly recorded cells in large-scale multielectrode recordings. *J Neurosci* 35: 4663-4675, 2015.

Litke AM, Bezayiff N, Chichilnisky EJ, Cunningham W, Dabrowski W, Grillo AA, Grivich M, Grybos P, Hottowy P, Kachiguine S. What does the eye tell the brain?: Development of a system for the large-scale recording of retinal output activity. *Nuclear Science, IEEE Transactions on* 51: 1434-1440, 2004.

Liu C, Li Y, Peng M, Laties AM, Wen R. Activation of caspase-3 in the retina of transgenic rats with the rhodopsin mutation s334ter during photoreceptor degeneration. *J Neurosci* 19: 4778-4785, 1999.

MacLaren RE, Pearson RA, MacNeil A, Douglas RH, Salt TE, Akimoto M, Swaroop A, Sowden JC, Ali RR. Retinal repair by transplantation of photoreceptor precursors. *Nature* 444: 203-207, 2006.

Makiyama Y, Ooto S, Hangai M, Takayama K, Uji A, Oishi A, Ogino K, Nakagawa S, Yoshimura N. Macular cone abnormalities in retinitis pigmentosa with preserved central vision using adaptive optics scanning laser ophthalmoscopy. *PLoS One* 8: e79447, 2013.

Marc RE, Jones BW. Retinal remodeling in inherited photoreceptor degenerations. *Mol Neurobiol* 28: 139-147, 2003.

Margolis DJ, Detwiler PB. Cellular origin of spontaneous ganglion cell spike activity in animal models of retinitis pigmentosa. *J Ophthalmol* 2011: 2011.

Margolis DJ, Gartland AJ, Singer JH, Detwiler PB. Network oscillations drive correlated spiking of ON and OFF ganglion cells in the rd1 mouse model of retinal degeneration. *PLoS One* 9: e86253, 2014.

Margolis DJ, Newkirk G, Euler T, Detwiler PB. Functional stability of retinal ganglion cells after degeneration-induced changes in synaptic input. *J Neurosci* 28: 6526-6536, 2008.

Marmarelis PZ, Naka K. White-noise analysis of a neuron chain: an application of the Wiener theory. *Science* 175: 1276-1278, 1972.

Marre O, Amodei D, Deshmukh N, Sadeghi K, Soo F, Holy TE, Berry MJ. Mapping a complete neural population in the retina. *J Neurosci* 32: 14859-14873, 2012.

Martinez-Navarrete G, Seiler MJ, Aramant RB, Fernandez-Sanchez L, Pinilla I, Cuenca N. Retinal degeneration in two lines of transgenic S334ter rats. *Exp Eye Res* 92: 227-237, 2011.

Masland RH. The neuronal organization of the retina. *Neuron* 76: 266-280, 2012.

Mastronarde DN. Correlated firing of cat retinal ganglion cells. I. Spontaneously active inputs to X- and Y-cells. *J Neurophysiol* 49: 303-324, 1983.

Mayhew TM, Astle D. Photoreceptor number and outer segment disk membrane surface area in the retina of the rat: stereological data for whole organ and average photoreceptor cell. *J Neurocytol* 26: 53-61, 1997.

Mazzoni F, Novelli E, Strettoi E. Retinal ganglion cells survive and maintain normal dendritic morphology in a mouse model of inherited photoreceptor degeneration. *J Neurosci* 28: 14282-14292, 2008.

Menzler J, Channappa L, Zeck G. Rhythmic ganglion cell activity in bleached and blind adult mouse retinas. *PLoS One* 9: e106047, 2014.

Menzler J, Zeck G. Network oscillations in rod-degenerated mouse retinas. *J Neurosci* 31: 2280-2291, 2011.

Mohand-Said S, Deudon-Combe A, Hicks D, Simonutti M, Forster V, Fintz AC, Léveillard T, Dreyfus H, Sahel JA. Normal retina releases a diffusible factor stimulating cone survival in the retinal degeneration mouse. *Proc Natl Acad Sci U S A* 95: 8357-8362, 1998.

Mohand-Said S, Hicks D, Simonutti M, Tran-Minh D, Deudon-Combe A, Dreyfus H, Silverman MS, Ogilvie JM, Tenkova T, Sahel J. Photoreceptor transplants increase host cone survival in the retinal degeneration (rd) mouse. *Ophthalmic Res* 29: 290-297, 1997.

Oesch N, Euler T, Taylor WR. Direction-selective dendritic action potentials in rabbit retina. *Neuron* 47: 739-750, 2005.

Openshaw A, Branham K, Heckenlively JR. Understanding Retinitis Pigmentosa. 2008.

Ortín-Martínez A, Jiménez-López M, Nadal-Nicolás FM, Salinas-Navarro M, Alarcón-Martínez L, Sauvé Y, Villegas-Pérez MP, Vidal-Sanz M, Agudo-Barriuso M. Automated quantification and topographical distribution of the whole population of S- and L-cones in adult albino and pigmented rats. *Invest Ophthalmol Vis Sci* 51: 3171-3183, 2010.

Ou J, Vijayasarathy C, Ziccardi L, Chen S, Zeng Y, Marangoni D, Pope JG, Bush RA, Wu Z, Li W, Sieving PA. Synaptic pathology and therapeutic repair in adult retinoschisis mouse by AAV-RS1 transfer. *J Clin Invest* 125: 2891-2903, 2015.

Oyster CW, Barlow HB. Direction-selective units in rabbit retina: distribution of preferred directions. *Science* 155: 841-842, 1967.

Park SP, Lee W, Bae EJ, Greenstein V, Sin BH, Chang S, Tsang SH. Early structural anomalies observed by high-resolution imaging in two related cases of autosomal-dominant retinitis pigmentosa. *Ophthalmic Surg Lasers Imaging Retina* 45: 469-473, 2014.

Petrusca D, Grivich MI, Sher A, Field GD, Gauthier JL, Greschner M, Shlens J, Chichilnisky EJ, Litke AM. Identification and characterization of a Y-like primate retinal ganglion cell type. *J Neurosci* 27: 11019-11027, 2007.

Pierce EA, Bennett J. The Status of RPE65 Gene Therapy Trials: Safety and Efficacy. *Cold Spring Harb Perspect Med* 5: a017285, 2015.

Prentice JS, Homann J, Simmons KD, Tkacik G, Balasubramanian V, Nelson PC. Fast, scalable, Bayesian spike identification for multi-electrode arrays. *PLoS One* 6: e19884, 2011.

Pu M, Xu L, Zhang H. Visual response properties of retinal ganglion cells in the royal college of surgeons dystrophic rat. *Invest Ophthalmol Vis Sci* 47: 3579-3585, 2006.

Puthussery T, Gayet-Primo J, Pandey S, Duvoisin RM, Taylor WR. Differential loss and preservation of glutamate receptor function in bipolar cells in the rd10 mouse model of retinitis pigmentosa. *Eur J Neurosci* 29: 1533-1542, 2009.

Puthussery T, Taylor WR. Functional changes in inner retinal neurons in animal models of photoreceptor degeneration. *Adv Exp Med Biol* 664: 525-532, 2010.

Ray A, Sun GJ, Chan L, Grzywacz NM, Weiland J, Lee EJ. Morphological alterations in retinal neurons in the S334ter-line3 transgenic rat. *Cell Tissue Res* 339: 481-491, 2010.

Rosenfeld PJ, Cowley GS, McGee TL, Sandberg MA, Berson EL, Dryja TP. A null mutation in the rhodopsin gene causes rod photoreceptor dysfunction and autosomal recessive retinitis pigmentosa. *Nature genetics* 1: 209-213, 1992.

Rossi J, Balthasar N, Olson D, Scott M, Berglund E, Lee CE, Choi MJ, Lauzon D, Lowell BB, Elmquist JK. Melanocortin-4 receptors expressed by cholinergic neurons regulate energy balance and glucose homeostasis. *Cell Metab* 13: 195-204, 2011.

Sagdullaev BT, McCall MA. Stimulus size and intensity alter fundamental receptive-field properties of mouse retinal ganglion cells in vivo. *Vis Neurosci* 22: 649-659, 2005.

Sandberg MA, Sullivan PL, Berson EL. Temporal aspects of the dark-adapted cone a-wave in retinitis pigmentosa. *Invest Ophthalmol Vis Sci* 21: 765-769, 1981.

Sanes JR, Masland RH. The types of retinal ganglion cells: current status and implications for neuronal classification. *Annu Rev Neurosci* 38: 221-246, 2015.

Sekirnjak C, Jepson LH, Hottowy P, Sher A, Dabrowski W, Litke AM, Chichilnisky EJ. Changes in physiological properties of rat ganglion cells during retinal degeneration. *J Neurophysiol* 105: 2560-2571, 2011.

Shin JA, Eom YS, Yu WQ, Grzywacz NM, Craft CM, Lee EJ. TIMP-1 affects the spatial distribution of dendritic processes of second-order neurons in a rat model of Retinitis Pigmentosa. *Exp Eye Res* 140: 41-52, 2015.

Shin JA, Kim HS, Vargas A, Yu WQ, Eom YS, Craft CM, Lee EJ. Inhibition of Matrix Metalloproteinase 9 Enhances Rod Survival in the S334ter-line3 Retinitis Pigmentosa Model. *PLoS One* 11: e0167102, 2016.

Shlens J, Field GD, Gauthier JL, Grivich MI, Petrusca D, Sher A, Litke AM, Chichilnisky EJ. The structure of multi-neuron firing patterns in primate retina. *J Neurosci* 26: 8254-8266, 2006.

Stasheff SF. Emergence of sustained spontaneous hyperactivity and temporary preservation of OFF responses in ganglion cells of the retinal degeneration (rd1) mouse. *J Neurophysiol* 99: 1408-1421, 2008.

Stasheff SF, Shankar M, Andrews MP. Developmental time course distinguishes changes in spontaneous and light-evoked retinal ganglion cell activity in rd1 and rd10 mice. *J Neurophysiol* 105: 3002-3009, 2011.

Steinberg RH. Survival factors in retinal degenerations. *Curr Opin Neurobiol* 4: 515-524, 1994.

Strettoi E. A Survey of Retinal Remodeling. *Front Cell Neurosci* 9: 494, 2015.

Strettoi E, Pignatelli V, Rossi C, Porciatti V, Falsini B. Remodeling of second-order neurons in the retina of rd/rd mutant mice. *Vision research* 43: 867-877, 2003.

Strettoi E, Porciatti V, Falsini B, Pignatelli V, Rossi C. Morphological and functional abnormalities in the inner retina of the rd/rd mouse. *The Journal of neuroscience* 22: 5492-5504, 2002.

Sümbül U, Song S, McCulloch K, Becker M, Lin B, Sanes JR, Masland RH, Seung HS. A genetic and computational approach to structurally classify neuronal types. *Nat Commun* 5: 3512, 2014.

Sun W, Li N, He S. Large-scale morophological survey of rat retinal ganglion cells. *Vis Neurosci* 19: 483-493, 2002.

Tian N, Copenhagen DR. Visual stimulation is required for refinement of ON and OFF pathways in postnatal retina. *Neuron* 39: 85-96, 2003.

Toychiev AH, Ivanova E, Yee CW, Sagdullaev BT. Block of gap junctions eliminates aberrant activity and restores light responses during retinal degeneration. *J Neurosci* 33: 13972-13977, 2013.

Trenholm S, Awatramani GB. Origins of spontaneous activity in the degenerating retina. *Front Cell Neurosci* 9: 277, 2015.

Trenholm S, Borowska J, Zhang J, Hoggarth A, Johnson K, Barnes S, Lewis TJ, Awatramani GB. Intrinsic oscillatory activity arising within the electrically coupled AII amacrine-ON cone bipolar cell network is driven by voltage-gated Na+ channels. *J Physiol* 590: 2501-2517, 2012.

Trenholm S, Johnson K, Li X, Smith RG, Awatramani GB. Parallel mechanisms encode direction in the retina. *Neuron* 71: 683-694, 2011.

Troy JB. Spatial contrast sensitivities of X and Y type neurones in the cat's dorsal lateral geniculate nucleus. *J Physiol* 344: 399-417, 1983.

Tucker BA, Park I-H, Qi SD, Klassen HJ, Jiang C, Yao J, Redenti S, Daley GQ, Young MJ. Transplantation of adult mouse iPS cell-derived photoreceptor precursors restores retinal structure and function in degenerative mice. *PloS one* 6: e18992, 2011.

Ullman S. *The Interpretation of Visual Motion (Artificial Intelligence)*. The MIT Press, 1979

Vaney DI, Sivyer B, Taylor WR. Direction selectivity in the retina: symmetry and asymmetry in structure and function. *Nature Reviews Neuroscience* 13: 194-208, 2012.

Vaney DI. Territorial organization of direction-selective ganglion cells in rabbit retina. *J Neurosci* 14: 6301-6316, 1994.

Wassle H, Peichl L, Boycott BB. Dendritic territories of cat retinal ganglion cells. *Nature* 292: 344-345, 1981.

Wassle H, Riemann HJ. The mosaic of nerve cells in the mammalian retina. *Proc R Soc Lond B Biol Sci* 200: 441-461, 1978.

Wei W, Elstrott J, Feller MB. Two-photon targeted recording of GFP-expressing neurons for light responses and live-cell imaging in the mouse retina. *Nat Protoc* 5: 1347-1352, 2010.

Yee CW, Toychiev AH, Ivanova E, Sagdullaev BT. Aberrant synaptic input to retinal ganglion cells varies with morphology in a mouse model of retinal degeneration. *J Comp Neurol* 522: 4085-4099, 2014.

Yee CW, Toychiev AH, Sagdullaev BT. Network deficiency exacerbates impairment in a mouse model of retinal degeneration. *Front Syst Neurosci* 6: 8, 2012.

Yilmaz M, Meister M. Rapid innate defensive responses of mice to looming visual stimuli. *Curr Biol* 23: 2011-2015, 2013.

Yoshida K, Watanabe D, Ishikane H, Tachibana M, Pastan I, Nakanishi S. A key role of starburst amacrine cells in originating retinal directional selectivity and optokinetic eye movement. *Neuron* 30: 771-780, 2001.

Yu WQ, Eom YS, Shin JA, Nair D, Grzywacz SX, Grzywacz NM, Craft CM, Lee EJ. Reshaping the Cone-Mosaic in a Rat Model of Retinitis Pigmentosa: Modulatory Role of ZO-1 Expression in DL-Alpha-Aminoadipic Acid Reshaping. *PLoS One* 11: e0151668, 2016.

Zhang Y, Kim IJ, Sanes JR, Meister M. The most numerous ganglion cell type of the mouse retina is a selective feature detector. *Proc Natl Acad Sci U S A* 109: E2391-8, 2012.

Zhu CL, Ji Y, Lee E-J, Grzywacz NM. Spatiotemporal pattern of rod degeneration in the S334ter-line-3 rat model of retinitis pigmentosa. *Cell and tissue research* 351: 29-40, 2013.

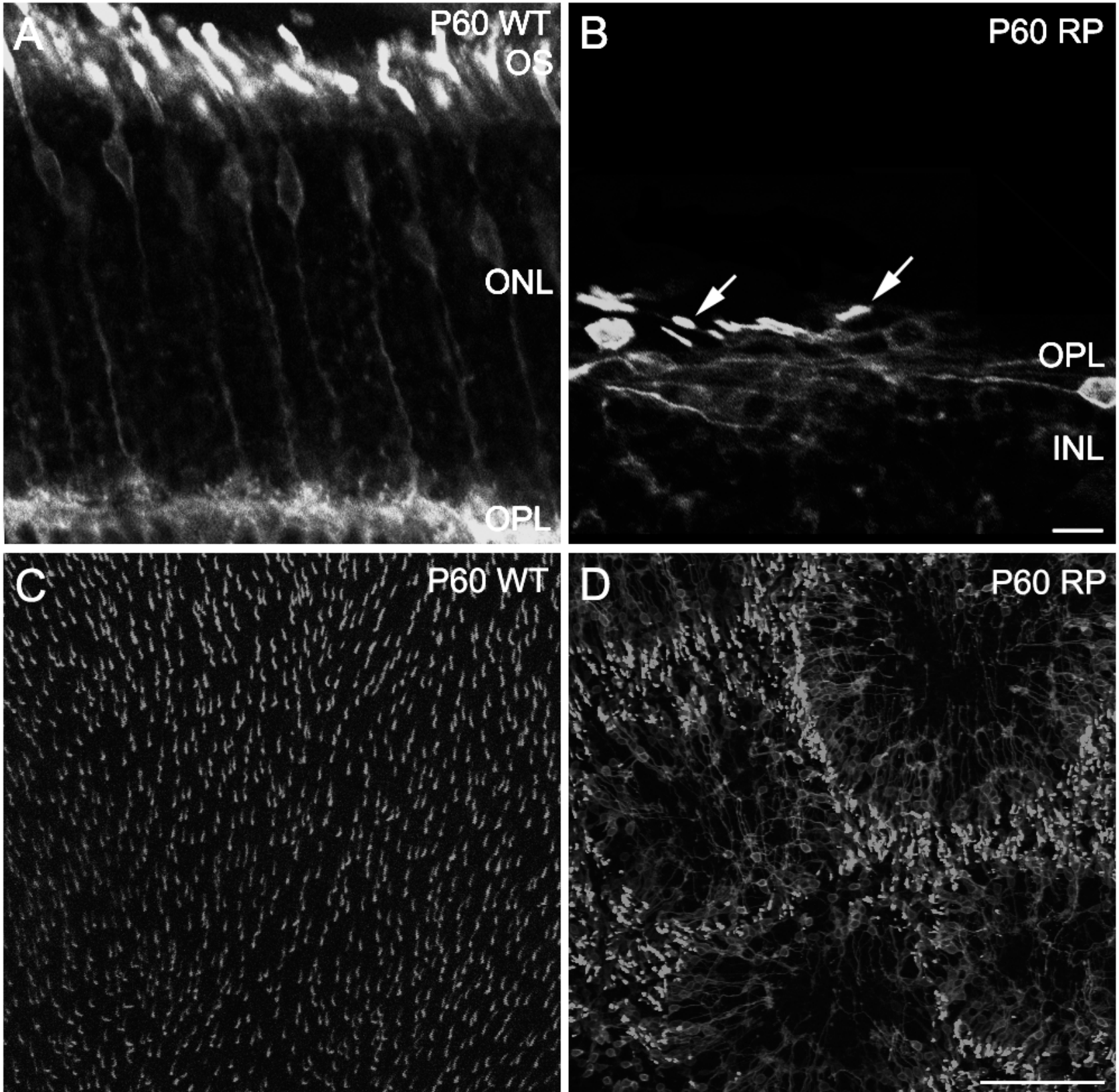
A
P60 WT
OS
ONL
OPL
B
P60 RP
OPL
INL
C
P60 WT
D
P60 RP

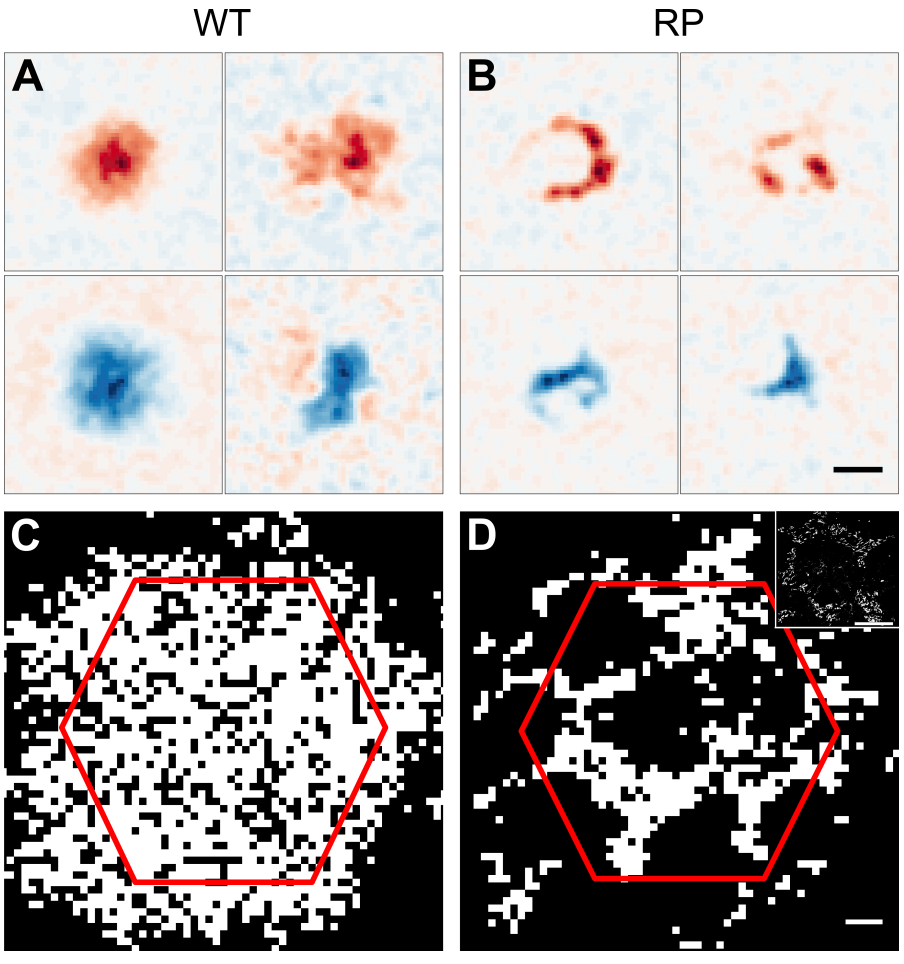
WT
RP
A
B
C
D

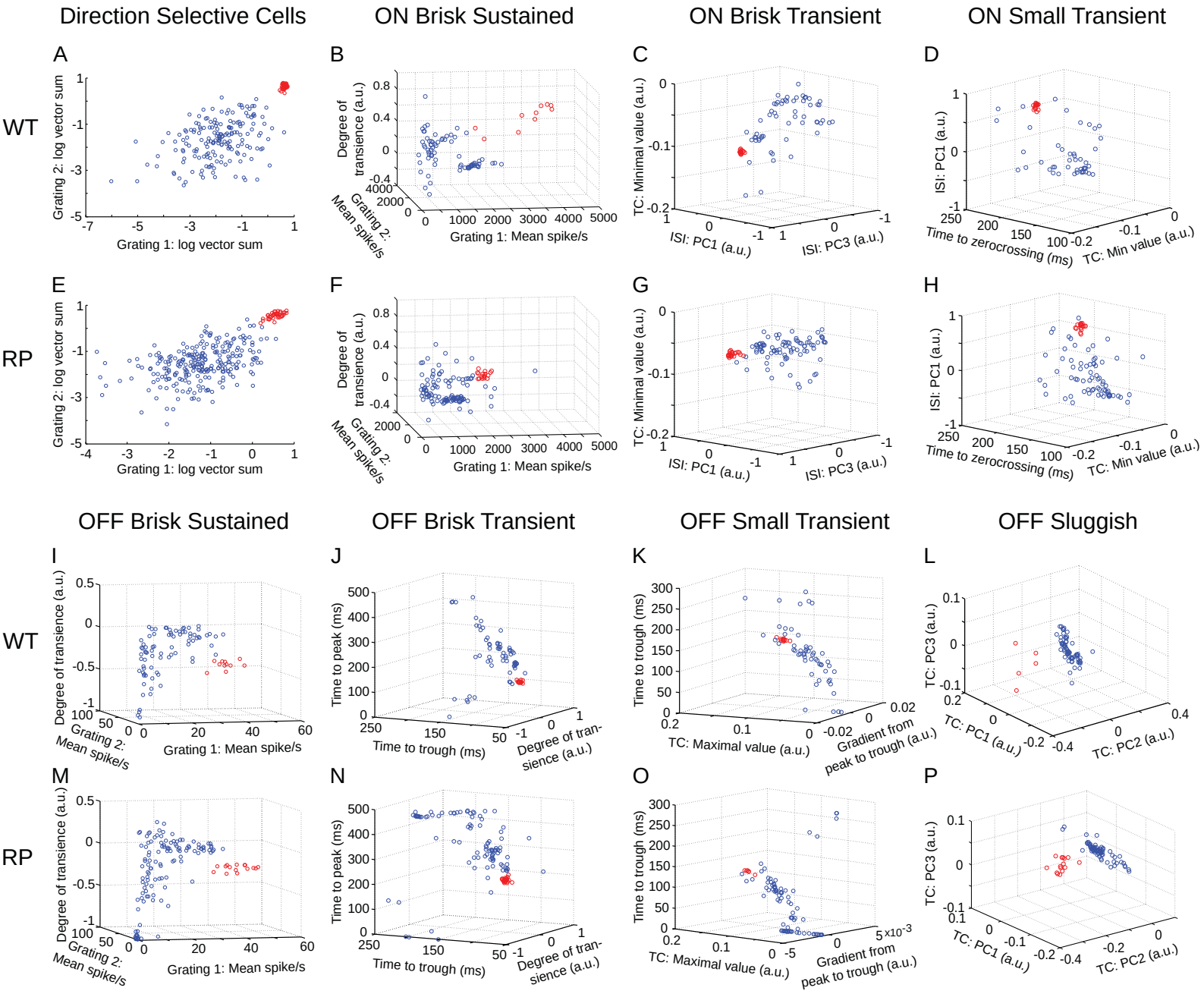
Direction Selective Cells
ON Brisk Sustained
ON Brisk Transient
ON Small Transient
WT
RP
A
B
C
D
E
F
G
H
Grating 2: log vector sum
Grating 1: log vector sum
Degree of transience (a.u.)
Grating 2: Mean spike/s
Grating 1: Mean spike/s
TC: Minimal value (a.u.)
ISI: PC1 (a.u.)
ISI: PC3 (a.u.)
Time to zerocrossing (ms)
TC: Min value (a.u.)
OFF Brisk Sustained
OFF Brisk Transient
OFF Small Transient
OFF Sluggish
I
J
K
L
M
N
O
P
Time to peak (ms)
Time to trough (ms)
Degree of transience (a.u.)
TC: Maximal value (a.u.)
Gradient from peak to trough (a.u.)
TC: PC1 (a.u.)
TC: PC2 (a.u.)
TC: PC3 (a.u.)

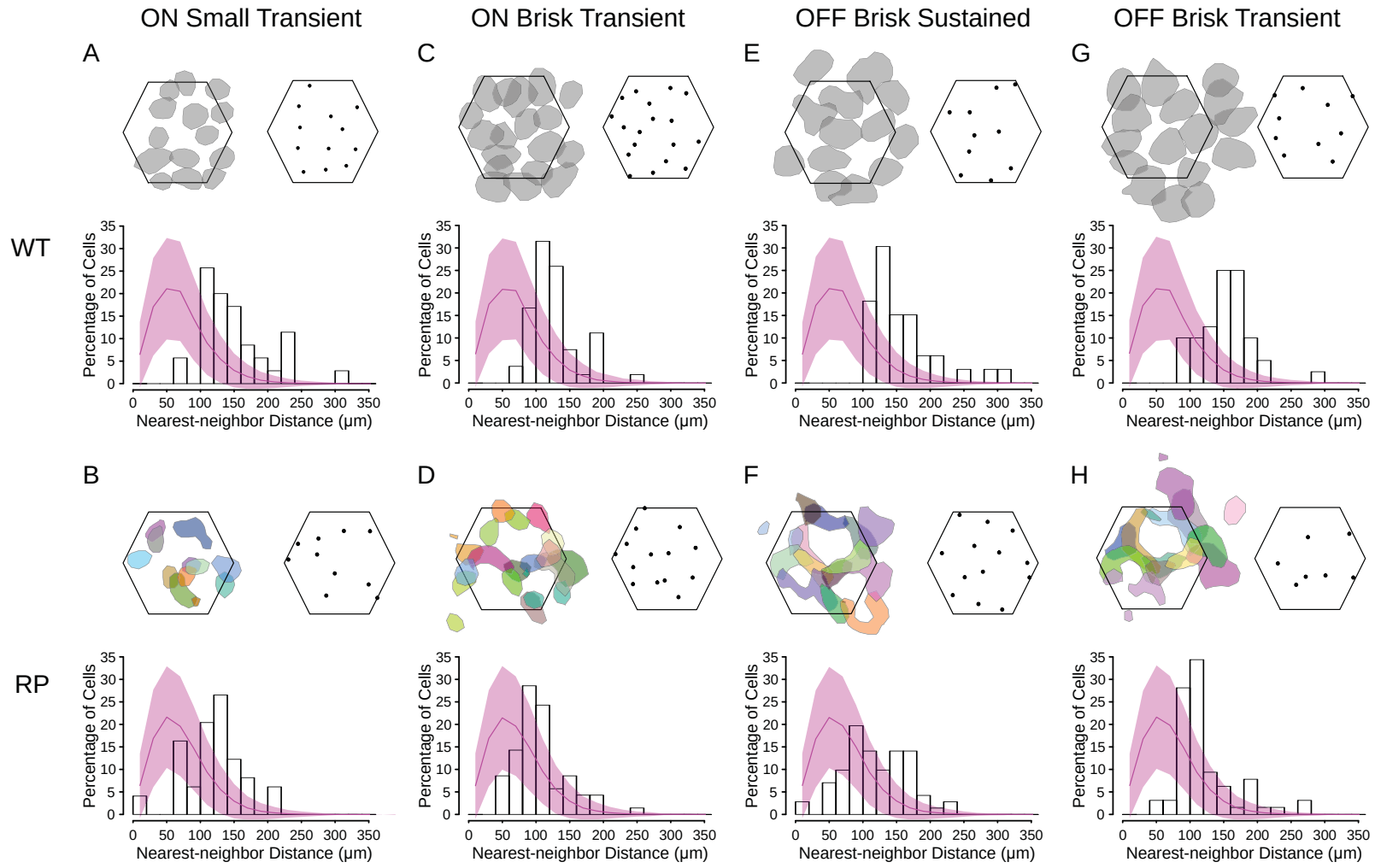
ON Small Transient
ON Brisk Transient
OFF Brisk Sustained
OFF Brisk Transient
A
C
E
G
B
D
F
H
WT
RP
Percentage of Cells
Nearest-neighbor Distance (µm)
0
5
10
15
20
25
30
35
0
50
100
150
200
250
300
350

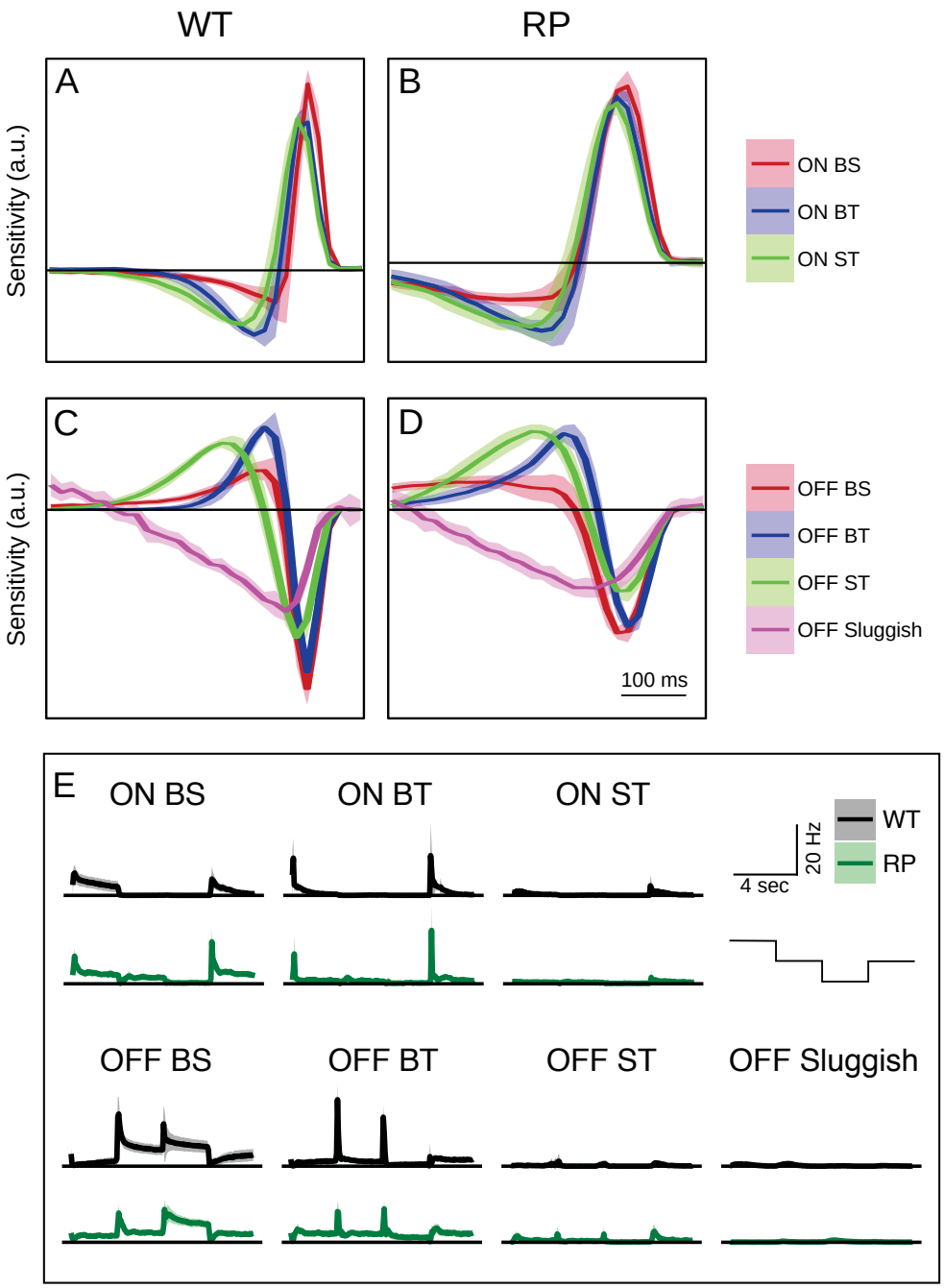
WT
RP
A
B
C
D
Sensitivity (a.u.)
Sensitivity (a.u.)
ON BS
ON BT
ON ST
OFF BS
OFF BT
OFF ST
OFF Sluggish
100 ms
E
ON BS
ON BT
ON ST
WT
RP
20 Hz
4 sec
OFF BS
OFF BT
OFF ST
OFF Sluggish

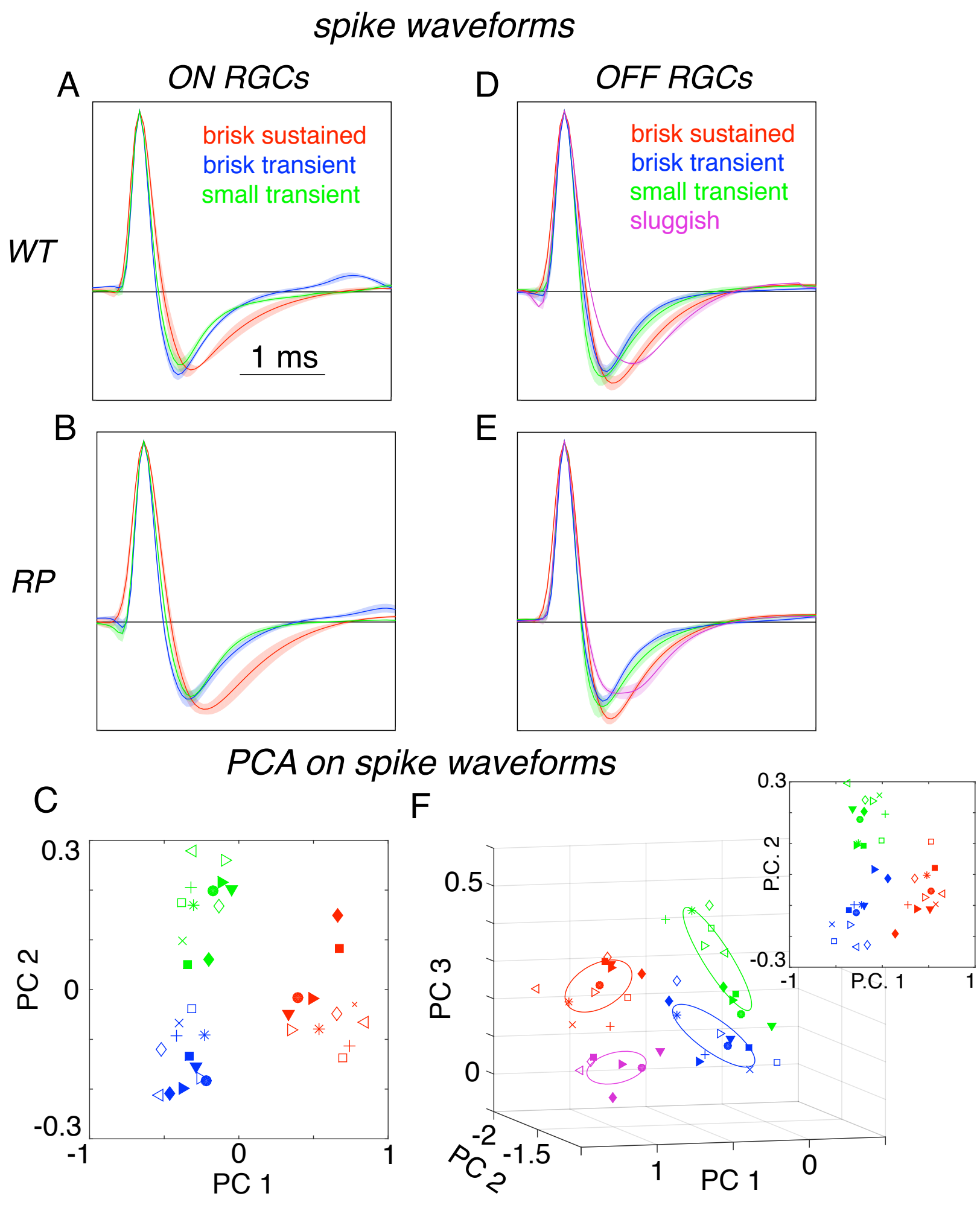
spike waveforms
A
ON RGCs
D
OFF RGCs
brisk sustained
brisk transient
small transient
sluggish
WT
1 ms
B
E
RP
PCA on spike waveforms
C
F
0.3
0
-0.3
PC 2
-1
0
1
PC 1
0.5
PC 3
-2
-1.5
PC 2
1
0
PC 1
P.C. 2
P.C. 1

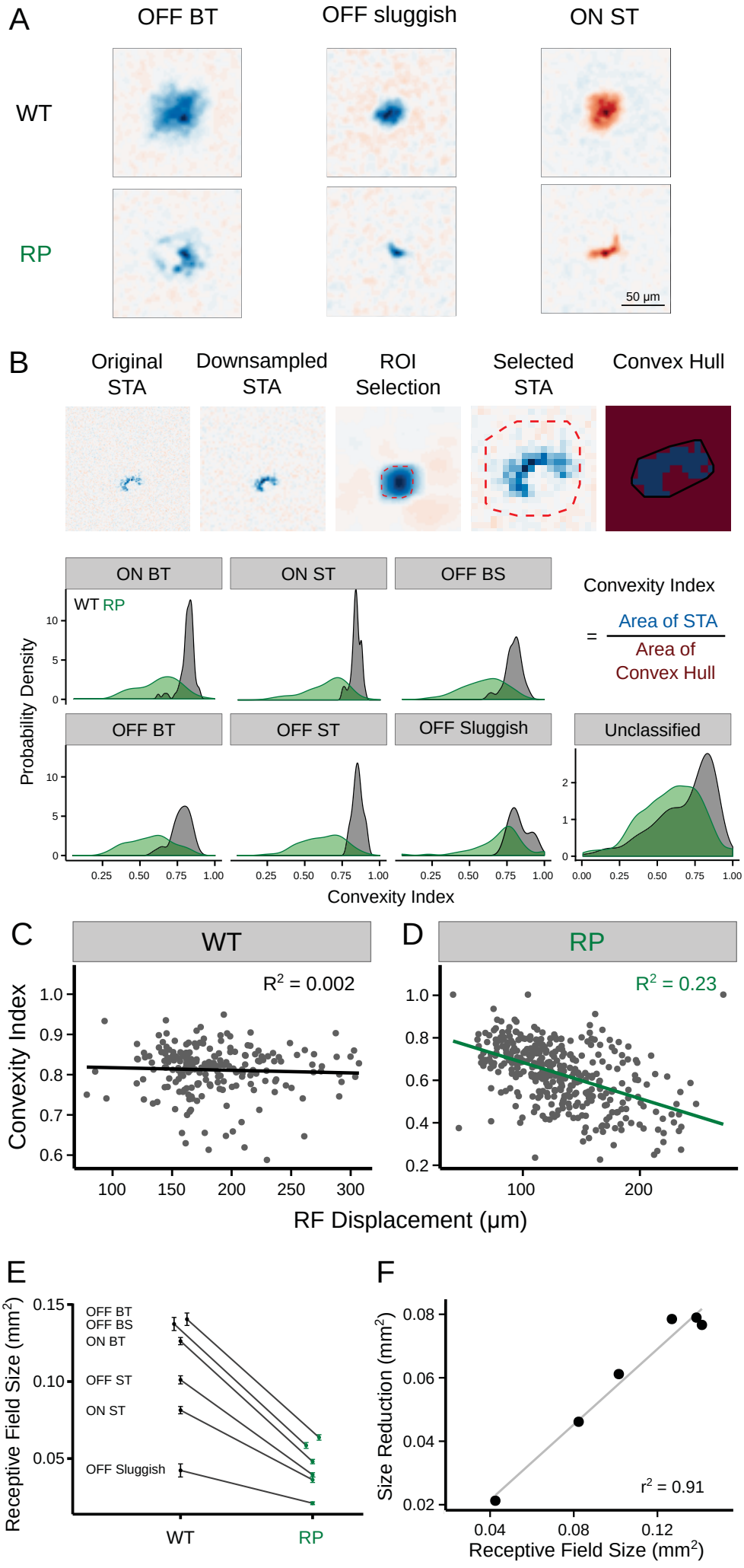
A
OFF BT
OFF sluggish
ON ST
WT
RP
50 µm
B
Original STA
Downsampled STA
ROI Selection
Selected STA
Convex Hull
ON BT
ON ST
OFF BS
WT RP
Probability Density
Convexity Index
= Area of STA / Area of Convex Hull
OFF BT
OFF ST
OFF Sluggish
Unclassified
Convexity Index
C
WT
R² = 0.002
Convexity Index
D
RP
R² = 0.23
RF Displacement (µm)
E
OFF BT
OFF BS
ON BT
OFF ST
ON ST
OFF Sluggish
Receptive Field Size (mm²)
WT
RP
F
Size Reduction (mm²)
r² = 0.91
Receptive Field Size (mm²)

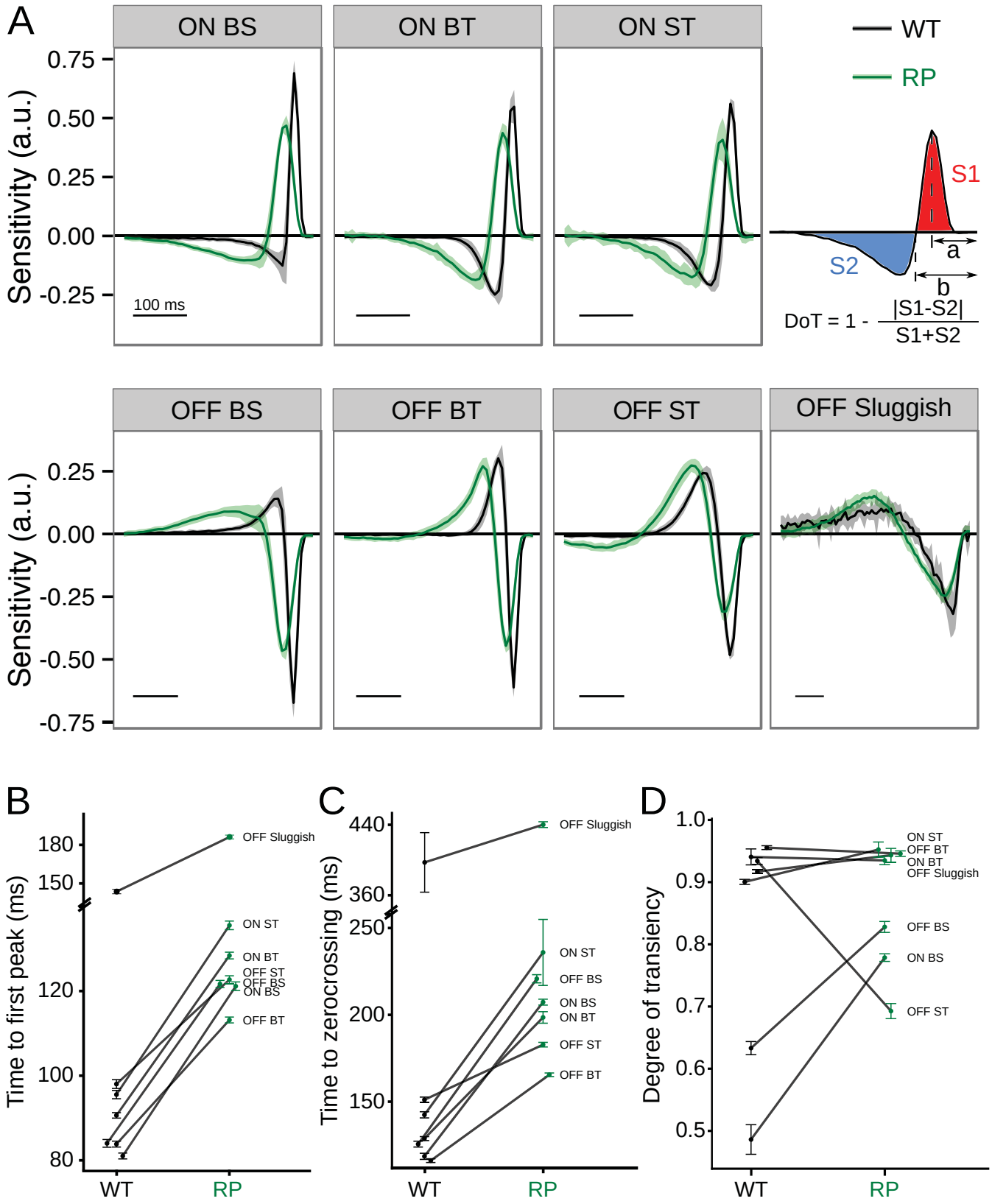
A
ON BS
ON BT
ON ST
WT
RP
Sensitivity (a.u.)
0.75
0.50
0.25
0.00
-0.25
100 ms
S1
S2
a
b
DoT = 1 - |S1-S2| / S1+S2
OFF BS
OFF BT
OFF ST
OFF Sluggish
0.25
0.00
-0.25
-0.50
-0.75
B
Time to first peak (ms)
180
150
120
100
80
OFF Sluggish
ON ST
ON BT
OFF ST
OFF BS
ON BS
OFF BT
WT
RP
C
Time to zerocrossing (ms)
440
360
250
200
150
OFF Sluggish
ON ST
OFF BS
ON BS
ON BT
OFF ST
OFF BT
WT
RP
D
Degree of transiency
1.0
0.9
0.8
0.7
0.6
0.5
ON ST
OFF BT
ON BT
OFF Sluggish
OFF BS
ON BS
OFF ST
WT
RP

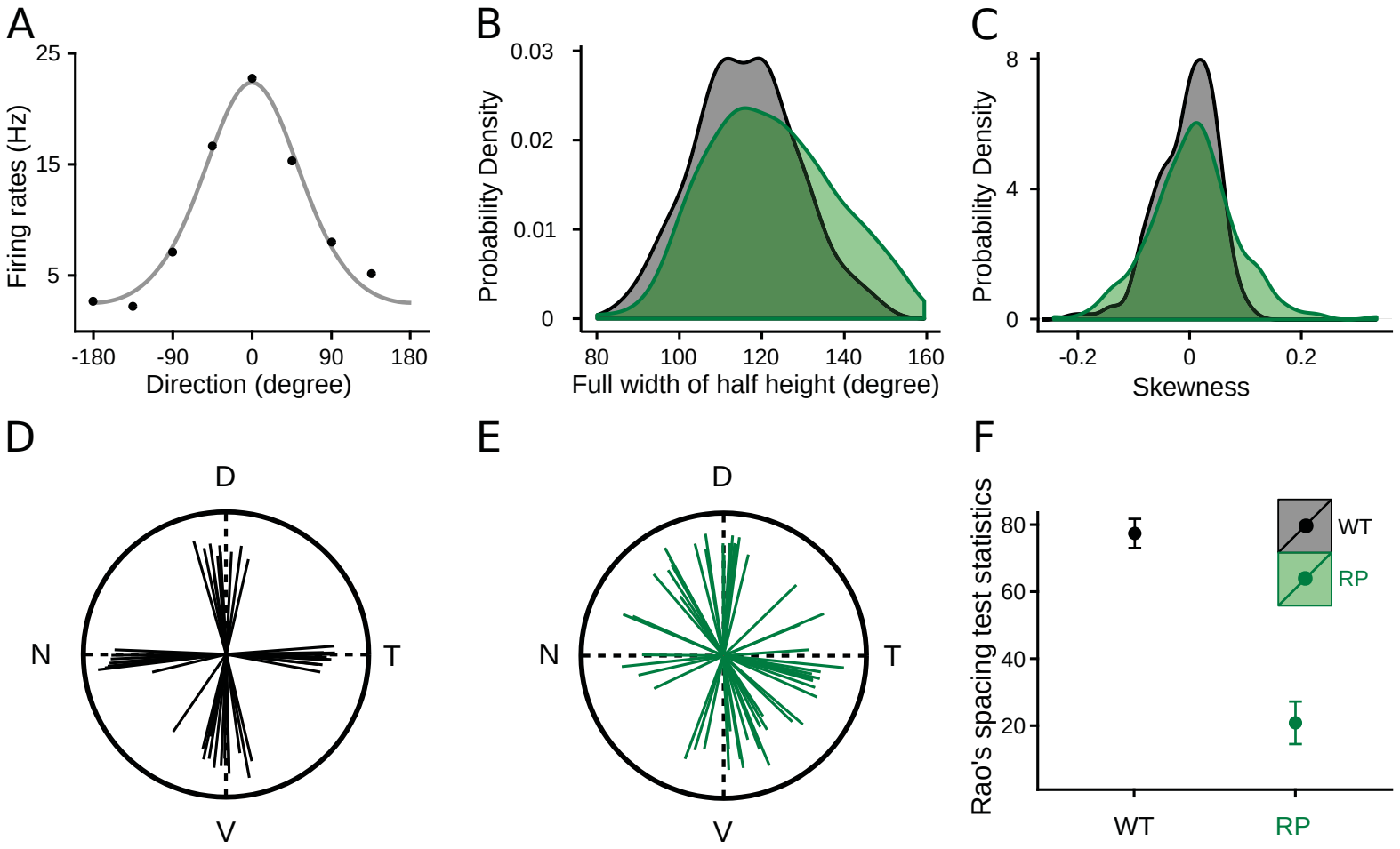
A
25
15
5
Firing rates (Hz)
-180
-90
0
90
180
Direction (degree)
B
0.03
0.02
0.01
0
Probability Density
80
100
120
140
160
Full width of half height (degree)
C
8
4
0
Probability Density
-0.2
0
0.2
Skewness
D
D
N
T
V
E
D
N
T
V
F
Rao's spacing test statistics
80
60
40
20
WT
RP
WT
RP

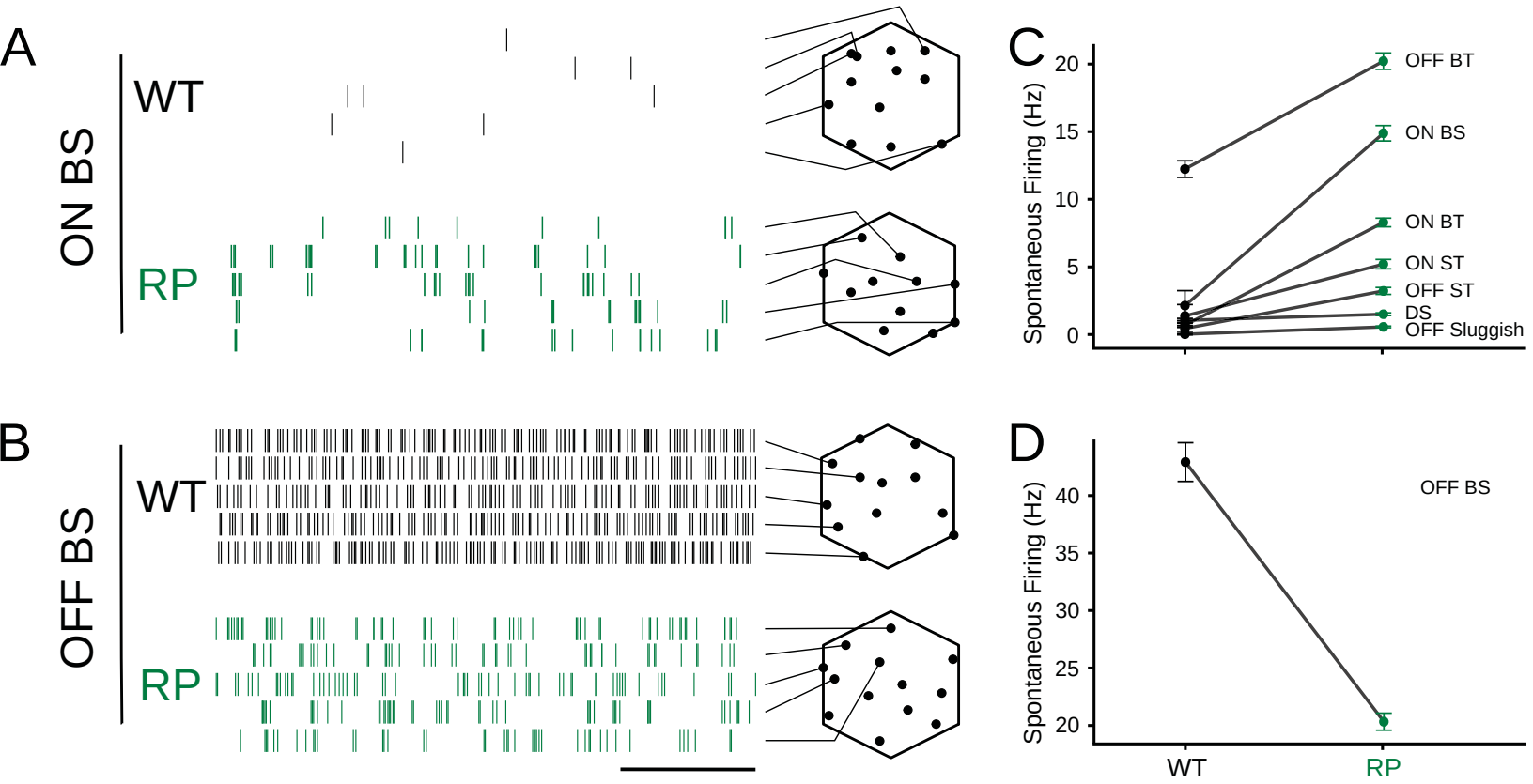
A
ON BS
WT
RP
C
Spontaneous Firing (Hz)
OFF BT
ON BS
ON BT
ON ST
OFF ST
DS
OFF Sluggish
B
OFF BS
WT
RP
D
Spontaneous Firing (Hz)
OFF BS
WT
RP

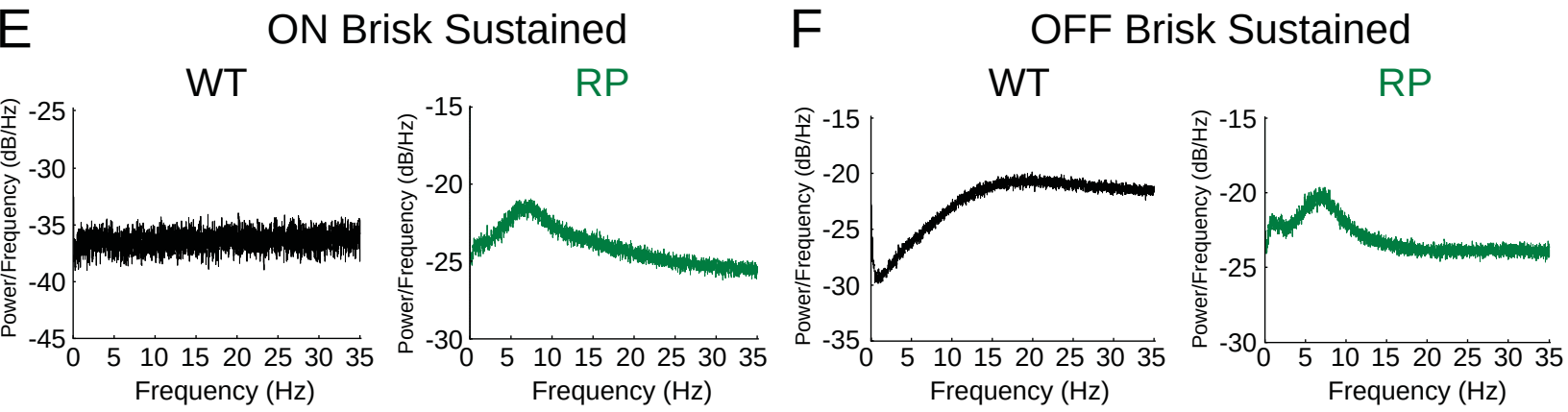
E
ON Brisk Sustained
WT
RP
F
OFF Brisk Sustained
WT
RP
Power/Frequency (dB/Hz)
Frequency (Hz)

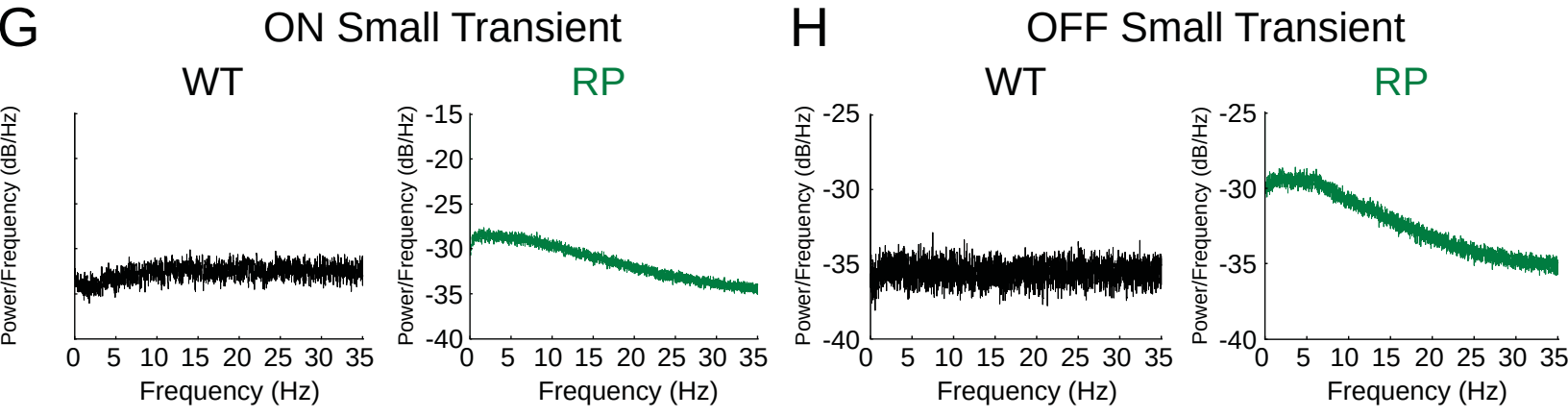
G
ON Small Transient
WT
RP
H
OFF Small Transient
WT
RP
Power/Frequency (dB/Hz)
Frequency (Hz)